ABSTRACT

Title of dissertation: A TIME-SERIES GEOCHEMICAL STUDY OF THE CA. 2.5 GA BATATAL FORMATION IN BRAZIL: SULFUR AND CARBON ISOTOPIC INSIGHTS INTO ENVIRONMENTAL CONDITIONS BEFORE THE GREAT OXIDATION EVENT

Iadviga Zhelezinskaia, Master of Science, 2013

Dissertation directed by: Professor Alan Jay Kaufman,
Department of Geology
Professor James Farquhar,
Department of Geology

Neoarchean metasedimentary rocks from the Batatal Formation, Brazil were studied using petrographic, elemental and stable isotopic techniques to provide a better understanding of coupling between the atmosphere-ocean system and biogeochemical cycles prior to the Great Oxidation Event. Multiple sulfur isotope data from both shale and carbonate lithofacies confirms global preservation of mass-independent fractionations, thought to be produced through photochemical reactions in an oxygen-free Neoarchean atmosphere. Isotopic differences between lithofacies within the shallow marine Batatal Formation, and beyond in deeper subtidal environments from correlative successions in Western Australia and South Africa, suggest a strong influence of environmental conditions on the preservation of distinct $\Delta^{33}S$ signatures. To explain the novel isotopic data, it is proposed the Batatal Formation was deposited in a shallow water evaporitic environment, which resulted

in higher sulfate concentrations and greater sulfur isotope fractionation associated with the activity of sulfate-reducing bacteria. Higher temperatures associated with such environments may have also promoted carbon dioxide limitation resulting in lesser carbon isotopic fractionation by photoautotrophs.

A TIME-SERIES GEOCHEMICAL STUDY OF THE CA. 2.5 GA BATATAL FORMATION IN BRAZIL: SULFUR AND CARBON ISOTOPIC INSIGHTS INTO ENVIRONMENTAL CONDITIONS BEFORE THE GREAT OXIDATION EVENT

by

Iadviga Zhelezinskaia

Thesis submitted to the Faculty of the Graduate School of the
University of Maryland, College Park in partial fulfillment
of the requirements for the degree of
Master of Science
2013

Advisory Committee:
Professor Alan Jay Kaufman, Chair/Advisor
Professor James Farquhar, Co-Advisor
Doctor Richard Ash

Acknowledgments

First, I would like to thank my spectacular advisors, Professors Alan Jay Kaufman and James Farquhar for giving me the chance to work on a challenging and interesting project over the last two years. Second, I would like to acknowledge the financial support from the Fulbright Program that let me come to the United States, and also from the Geological Society of America and the Department of Geology at the University of Maryland, College Park, for some contribution to the research.

I would like also to thank the people I worked with in the laboratory: Joost Hoek, Yongbo Peng, Rebecca Plummer, Zahra Mansaray, Jonathan Banker, Daniel Eldridge, Michael Antonelli, Huan Cui and Palma Jarboe. Thanks are due to Doctor Richard Ash for agreeing to serve on my thesis committee. Additional acknowledgement for Sergio Kolling from Anglo Gold Ashanti in Brazil who assisted Professor Jay Kaufman and Nick Geboy in the sampling of the Batatal core.

I owe my deepest thanks to my family in Russia who have always supported me through my career. Many thanks to my roommates Camli Badrya and Cesar Saenz for being my best friends in the United States and Hector Escobar for introducing me to the Latex computer program to write this manuscript.

Contents

List of Tables

List of Figures

Chapter 1

Introduction

The composition and evolution of Earth's early atmosphere has been a subject of great scientific interest. Research work on this project has focused on both the role of atmospheric evolution in climate and on the controls on its chemistry and oxidation state. Sagan and Mullen (1972) proposed the "faint young Sun" hypothesis, which describes contradictory evidence that there was liquid water on Earth at the same time that our star was only 70% as luminous as today. Other research, including two opposing models describing the Archean atmosphere have dominated scientific debate over the past 40 years: the first, that the atmosphere became progressively oxidizing around 2.4-2.0 Ga (Cloud, 1972; Holland, 1984; Kasting, 1987) in the so-called Great Oxidation Event (GOE) just after the Archean-Proterozoic boundary, and the second, that there was an oxidizing atmosphere as far back as 3.5 Ga (Dimroth and Kimberley, 1976; Ohmoto, 1996) near the beginning of the Archean Eon. These entrenched views were tested by the novel discovery of profound mass-independent fractionation (MIF) of sulfur isotopes in rocks older than $\sim$2.5 Ga by Farquhar and colleagues (Farquhar et al., 2000), which was interpreted as resulting from photochemical reactions of volcanic SO_2 in an anoxic atmosphere. Based on these observations, the greater majority of the scientific community now speaks confidently about a critical rise of oxygen across the Archean-Proterozoic

boundary.

Current studies of MIF genesis and preservation generally focus on either: 1. explanations for the anomalous signals (Farquhar et al., 2007, 2013; Lasaga et al., 2008; Oduro et al., 2011; Ohmoto et al., 2006; Ueno et al., 2009; Watanabe et al., 2009); 2. the asymmetry of the preserved isotopic record (Halevy et al., 2010); or 3. the facies-dependence of MIF within and between basins (Ono et al., 2009b).

This study of Neoarchean sedimentary rocks from the São Francisco Craton, Brazil was originally designed to test whether MIF events recorded in broadly equivalent Western Australia and South African basins were global in extent and could be used for correlation purposes. However, in the course of my investigation, I found strong evidence for important differences between facies that provide constraints on Neoarchean bacterial sulfate reduction and may provide a way to close the isotopic balance of the Archean sulfur cycle.

1.1 Characteristics of the Archean-Paleoproterozoic transition

The Archean-Proterozoic transition is arguably one of the most important intervals of planetary history in terms of Earth system changes. By the start of the Palaeoproterozoic Era, the process of cratonization, the growth and stabilization of the continental crust (McLennan and Taylor, 1982), is thought to have peaked and begun to slow (Condie and ONeill, 2010). At the same time, it has been proposed that plate tectonics was initiated (Nelson, 1998) causing the break up the supercontinents, widespread rifting events, mafic dyke swarms, and the formation

of large igneous provinces (LIPs). All these lines of evidences reflect tremendous changes in the Earth's interior, which may have influenced surface environments by the emission of large volumes of volcanic gases (CO_2, H_2S, SO_2) that could have driven atmospheric evolution. One of the sedimentary features of this period was the widespread deposition of banded iron formations (BIFs), platform carbonates, and black shales.

It is thought that in the Neoarchean Era two supercontinents existed: northern Kenorland (Williams et al., 1991) and southern Vaalbara (Cheney, 1996; de Kock et al., 2009). On the basis of sequence stratigraphy, Cheney (1996) proposed the existence of the Vaalbara supercontinent, including the Kaapvaal Province of South Africa and the Pilbara Province of northern Western Australia. Aspler and Chiarenzelli (1998) later suggested that Vaalbara may also include the São Francisco Craton in Brazil.

Barley and colleagues (Barley et al., 2005) proposed links between the rise of atmospheric oxygen and supercontinent formation, active magmatism, volcanic gas eruption and glaciation about 2.5 billion years ago. Another explanation for the dramatic change in oxygen levels was suggested by Kump and colleagues (Kump et al., 2001) who concluded that the type and oxidation state of volcanic gases changed through time because of mantle cooling. Alternatively, other studies concluded that basalts formed since 3.5 Ga and across the Archean-Proterozoic transition did not change their oxidation state (Canil, 2002) leading to speculation that changes in degassing pressure during volcanism could have driven the oxygenation of the Neoarchean atmosphere (Gaillard et al., 2011).

1.2 Geological and Geochemical Indicators of Temporal Redox Change

To understand past condition on Earth surface, I provide an overview of main redox indicators and their interpretations for Earth system history across the Archean-Proterozoic transition. This discussion will provide context for my time-series petrological and geochemical study of the Neoarchean Batatal Formation in Brazil.

1.2.1 Detrital Minerals

Because the surface environment is in direct contact with the atmosphere, rocks and sediments formed there may reflect its redox condition. For example, the minerals uraninite, pyrite and siderite are sensitive to redox state insofar as they are stable only under reducing conditions.

The first mineralogical evidence used to claim a reducing Archean atmosphere was the discovery of detrital uraninite and pyrite in the Witwatersrand basin of South Africa (Ramdohr, 1958). Holland (1984) calculated that ρO_2 must have been less than 10^{-2} of the present atmospheric level (PAL) for preservation of detrital uraninite. Detrital siderite, pyrite and other heavy minerals have also been found in the Pilbara Craton, Australia in sedimentary rocks older than 2.75 Ma (Rasmussen and Buick, 1999). The round shape of detrital mineral grains demonstrates long-term transport of minerals in streams; the preservation of these textures and absence of oxidation reactions led researchers to conclude that the atmosphere was oxygen-free at the time of deposition (see Holland (1984)). However, preservation of

rounded mineral grains may also be related to high sedimentation rates even under an oxidizing atmosphere.

1.2.2 Massive Sulfates and Red Beds

Red beds are clastic sediments with a matrix partially composed of oxidized iron-bearing minerals (predominantly hematite), which give these rocks a reddish color (Cloud, 1968). Notably, these types of rocks are observed in successions younger that ca. 2.3 Ga in South Africa (Eriksson and Cheney, 1992), North America (Bekker et al., 2006), and Fennoscandia (Melezhik et al., 1999), but not in similar sedimentary facies in older parts of these successions. Red bed deposition, then, may be a good indicator of an oxidizing atmosphere. It is believed that before the time of red bed deposition, iron was predominantly in form of soluble ferrous iron (Fe^{2+}), and it was thus mobile in solutions. However, when widespread surface oxygenation occurred, mobile ferrous iron oxidized to immobile ferric iron (Fe^{3+}) resulting in the cementation of sandstone accumulations with hematite forming red beds.

Massive sulfates are believed to be another indicator for oxidizing conditions. Massive sulfate deposits are only recognized in rocks younger than 2.1 Ga (Melezhik et al., 2005). The formation of massive sulfates typically occur at high level of SO_4^{2-} in evaporated seawater. Because dissolved seawater sulfate results primarily from the oxidative weathering of sulfides, massive sulfates would be rare when atmospheric oxygen levels were low. It is postulated that after oxygen rose in the atmosphere stimulating widespread oxidative weathering, the budget of sulfate in

seawater changed dramatically allowing for the deposition of massive sulfates.

1.2.3 Paleosols

Paleosols are ancient soil weathering profiles, which form in direct contact with the atmosphere and hence mirror atmospheric oxygen level at the time of formation. The limitations for using paleosols include their correct identification (for example, some hydrothermal alteration zones may appear similar to paleosols), the presence of homogeneous parent rocks, and their degree of preservation (Rye et al., 1998). Interpretation of atmospheric conditions based on the study of paleosols and parent rocks are largely based on the mobility of elements. Elements such as Al, Ti and Zr are usually immobile under weathering conditions, while Ca, Mg, Na, K and Mn are generally mobile (Nesbitt and Young, 1982). Hence the ratio of immobile to immobile elements can help to determine paleosols. Iron as a redox sensitive element is considered as an indicator of the oxidation state of the atmosphere. As mentioned above, under reducing conditions Fe^{2+} is mobile and tend to be removed from paleosols during their formation; alternatively, Fe^{3+} is retained in paleosols formed under an oxidizing atmosphere (Holland, 1984). Mobilized iron may then be precipitated in clays (e.g., smectite) or carbonates (siderite) in ancient soils. However, the preservation of iron carbonate also depends on the partial pressure of CO_2. At $\rho CO_2 \leq 10^{-1.7}$ siderite would be preserved (Rye et al., 1995), but in higher concentrations of this atmospheric gas, siderite would be unstable and likely to be removed by dissolution, as interpreted from a pre-2.2 Ga paleosol from Western

Australia (Rye et al., 1995).

1.2.4 Banded Iron Formation

Banded-Iron Formation (BIF) consists of layers of silica, iron oxides, iron carbonates, iron silicates, and rare bands of iron sulfides. BIFs are divided into two groups. The Algoma-type IFs are related to volcanogenic processes, and the Superior-type IFs have a sedimentary origin and are thought to form on continental margins (James, 1954; Melnik, 1982). The peak of Superior-type BIF deposition occured between 2.5 and 2.2 Ga, corresponding roughly to the time of the rise of atmospheric oxygen (Beukes and Gutzmer, 2008). The widespread deposition of iron formation suggests significant accumulation of ferrous iron in ocean water as well as precipitation of ferric iron resulting from oxidation reactions. The ultimate source of iron and silica for BIFs is thought to have been subaerial weathering and hydrothermal emissions from mid-ocean ridges (Derry and Jacobsen, 1990).

This study focuses on black shales from Minas Supergroup, Brazil that were deposited approximately 2.5 Ga and that are overlain by Cauê Banded-Iron Formation, a Superior type BIF. The Cauê IF is thought to be correlated with the similarly aged Kuruman IF in South Africa and Brockman IF in Western Australia (see Fig. 2.5).

1.2.5 Trace Elements

Redox sensitive elements such as V, Mo, U, Re, and Mn are variably soluble or insoluble under oxic or anoxic conditions and are very sensitive to the availability of O_2 in the water column. The relative abundance of these redox-sensitive trace elements have been used to estimate water column oxygen levels (Morford and Emerson, 1999).

Molybdenum is soluble as the oxidized molybdate (MoO_4^{2-}) ion and is absorbed by seafloor Mn and Fe oxides resulting in both sediment Mo enrichment and Mo isotope fractionation (Barling and Anbar, 2004; Barling et al., 2001). Molybdate can be converted to oxythiomolybdates ($MoO_{(4-x)}S_x^{2-}$) in a reaction with HS^- and co-precipitate with iron sulfides in anoxic (sulfidic) conditions (Vorlicek et al., 2004). This behavior of molybdenum, molybdate, and thiomolybdate provides the basis for the suggestion that Mo enrichment in 2.5 Ga black shales from Australia provide evidence for a "whiff" of atmospheric oxygen tens to hundreds of million of years before the Great Oxidation Event. The whiff is speculated to have resulted in the weathering of exposed sulfide minerals, which subsequently mobilized molybdenum as molybdate to be transported into the oceans where the shales were deposited (Anbar et al., 2007). The horizon S1 in the Mt. McRae Shale Formation preserves elevated Re and Mo concentrations that have been interpreted to indicate slightly oxidizing surface conditions, which were high enough to mobilize Re and Mo as oxyanions, ultimately leading them to their transfer to the sedimentary record. In contrast to molybdenum and rhenium, uranium does not show any change in

concentration across the same stratigraphic interval. This has been interpreted to reflect the fact that uranium is principally a constituent of silicates (feldspar, titanite, zircon, etc.) and phosphate minerals (e.g. apatite) but not sulfides. Anbar et al. (2007) concluded that the oxygen level at the time the Mt. McRae Shale Formation was deposited was insufficient to weather U-containing minerals to make uranium mobile, but was high enough to oxidized sulfides and to form oxyanions of Mo and Re. Anbar et al. (2007) used experimental evidence to argue that the rate of pyrite oxidation at this time exceeded that of feldspar minerals when $\rho O_2 \leq 10^{-6}$ PAL, supporting the whiff of oxygen interpretation. Simply stated, small temporal oxygen rise occurred even before the Great Oxidation Event. The source of this oxygen may reflect the appearence of cyanobacteria, which is thought to have occured at approximately 2.7 Ga (Brocks et al., 1999).

1.3 The Great Oxidation Event

The single greatest transformation in the oxidation state of Earth's atmosphere has come to be known as the Great Oxidation Event (GOE). Holland (1984) conceived of this name and assigned this event to a time between approximately 2.0 and 2.3 Ga. The reason for a such tremendous change in Earth's atmospheric oxidation state is debated, but it appears most likely that it was linked to the evolution of oxygenic photosynthesis (Kopp et al., 2005) by the establishment of widespread cyanobacterial activity or photosynthetic eukaryotes (Guo et al., 2009). Brocks et al. (1999) found evidence for photosynthesis ∼2.7 Ga in the Pilbara Craton, Australia

(recently, this biomarker evidence was questioned by Rasmussen et al. (2008)). If correct, cyanobacteria already existed about 500 Ma before the GOE. If photosynthesis originated several hundred million years before the rise of oxygen, then a reason for the delay in surface oxidation is needed. It has been suggested that the phase of lag between the GOE and the first photosynthetically produced bacteria reflects buffering of the atmosphere and oceans by oxidation reactions.

1.4 Perturbations in the Carbon Cycle: Lomagundi Anomaly

The observation of anomalously positive $\delta^{13}C$ values in 2.0 - 2.2 Ga Lomagundi carbonates by Schidlowski et al. (1976) and of similar anomalies preserved elsewhere (Bekker et al., 2001; Guo et al., 2009; Karhu and Holland, 1996) has been linked to the early Paleoproterozoic rise of oxygen.

Carbon is an essential element for organic molecules, that occurs in seawater as bicarbonate, carbonate, and carbonic acid, in rocks as carbonate minerals and graphite, and in the atmosphere as carbon dioxide (CO_2), methane (CH_4), and various other carbon-bearing gases.

Carbon has two stable isotopes: ^{12}C and ^{13}C with natural abundances of 98.89% and 1.11%, respectively (Coplen et al., 2002), and variations in the carbon isotopic compositions are reported using the delta notation (δ), a ratio of isotopes in sample to the same ration in standard material. For carbon isotopes standard is

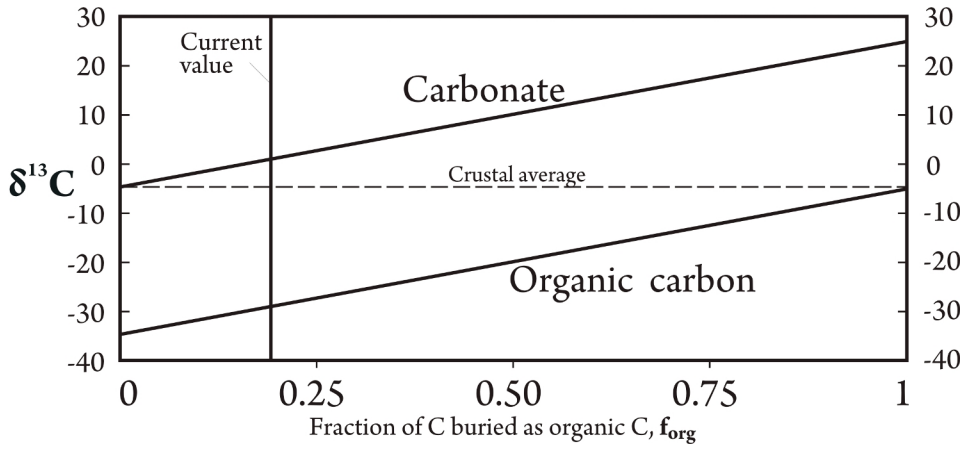

Figure 1.1: Open system behavior of carbon-bearing phases in seawater showing evolution of isotopic compositioms as a function of the fraction of carbon buried as organic matter. After (Des Marais, 2001)

the Pee Dee Belemnite (PDB) from the Pee Dee Formation in South Carolina:

$$\delta^{13}C = \left(\frac{\frac{^{13}C}{^{12}C}sample}{\frac{^{13}C}{^{12}C}standard} - 1 \right) \times 1000 \tag{1.1}$$

Throughout much of the Earth history sedimentary carbonate rocks, such as dolomite and calcite, usually have $\delta^{13}C$ values close to zero (Coplen et al., 2002), reflecting the isotopic composition of dissolved inorganic carbon (DIC: carbonate, bicarbonate, and carbonic acid) in the seawater from which they precipitated.

The isotopic composition of seawater and thus carbonates depend on burial rate of organic matter (OM) (Des Marais, 2001) (see Fig. 1.1). Living organisms tend to preferentially accumulate lighter isotope ^{12}C for building organic molecules, resulting in significantly negative $\delta^{13}C$ values. The burial rate of OM determines how much ^{12}C is removed from the dissolved inorganic carbon pool in seawater. Higher fluxes of organic carbon burial result in more positive $\delta^{13}C$ values for DIC in

seawater and in turn for carbonates that precipitate from seawater. Karhu and Holland (1996) concluded that the global record of positive $\delta^{13}C$ in 2.0-2.2 Ga marine carbonates provides evidences for high burial rates of photosynthetically produced organic matter during this biogeochemical anomaly. If correct, photosynthesis implies production of significant quantities of oxygen, which provides a link to the GOE:

$$CO_2 + H_2O \longrightarrow CH_2O + O_2 \tag{1.2}$$

The isotopic composition of organic matter can be shifted by different processes and depends on many factors. The main factors for modern photosynthetic phytoplankton are believed to include: 1. cell geometry (Popp et al., 1998); 2. availability of nutrients; and 3. CO_2 concentration.

The most pronounced effect is thought to be the concentration of carbon dioxide in the atmosphere and therefore in the ocean. Experiments on marine diatoms demonstrated that the magnitude of carbon isotopic fractionation is inversely related to CO_2 concentration (Laws et al., 1997). Because concentration of dissolved CO_2 in the shallow water column depends on the partial pressure of carbon dioxide in the atmosphere and temperature, latitudinal variations in $\delta^{13}C$ of particulate organic matter at the ocean surface are observed and are consistent with experimental data (Goericke and Fry, 1994). At higher latitudes temperature decreases and solubility of CO_2 increases with the observation of more negative $\delta^{13}C$ of plankton organic matter (Goericke and Fry, 1994; Rau et al., 1989). Thus, at equator where ocean surface temperatures are highest, $\delta^{13}C$ values of plankton average around -20‰,

whereas at high latitudes ($> 60°$) $\delta^{13}C$ decrease to as low as -35‰.

1.5 Multiple Sulfur Isotopic Systematics

Sulfur plays an important role in elemental and biogeochemical cycles on the Earth today and may have been even more important in the geologic past. Sulfur exists in chemical compounds with oxidation states ranging from +6 to -2. In the Modern ocean sulfur exists primary as sulfate (oxidation state +6), which is the second most abundant anion with a concentration of 28 mmol/kg; it is conservative insofar as the SO_4^{2-}/Cl^- is constant throughout the present-day ocean masses, although this may not have been the case in the ancient past.

Sulfur is a constituent in evaporitic minerals such as gypsum, anhydrite, and barite, and also in sulfide minerals such as pyrite, pyrrhotite, greigite, mackinawite. In the atmosphere, sulfur is present as sulfur dioxide, sulfuric acid, elemental sulfur, hydrogen sulfide, and a variety of organic sulfur compounds.

Sulfur has four stable isotopes with variable natural abundances: $^{32}S = 94.93\%$, ^{33}S=0.76%, ^{34}S=4.29%, and ^{36}S=0.02% (Coplen et al., 2002). The sulfur isotopic composition of natural materials are most commonly reported using delta notation (δ):

$$\delta^{34}S = \left(\frac{\frac{^{34}S}{^{32}S}sample}{\frac{^{34}S}{^{32}S}std} - 1 \right) \times 1000 \tag{1.3}$$

$$\delta^{33}S = \left(\frac{\frac{^{33}S}{^{32}S}sample}{\frac{^{33}S}{^{32}S}std} - 1 \right) \times 1000 \tag{1.4}$$

$$\delta^{36}S = \left(\frac{\frac{^{36}S}{^{32}S}sample}{\frac{^{36}S}{^{32}S}std} - 1 \right) \times 1000 \tag{1.5}$$

The δ^{34}S value of Modern oceanic sulfate is approximately +21‰(Rees et al., 1978). The sulfate concentration in ocean water is thought to depend in part on atmospheric oxygen levels because sulfate is a product of sulfide oxidation during continental weathering. The concentration of sulfate in seawater is also controlled by sinks associated with the transformation of sulfate into sulfide by bacteria, which forms pyrite that is buried in sediments, and also the accumulation of evaporite deposits.

1.5.1 Mass-Dependent Isotope Fractionation Processes

Mass-dependent isotope fractionation processes arise because the primary control from differences between masses of different isotopes (Young et al., 2002). Equilibrium isotope effects arise in large part because different vibrational frequencies of different isotopes in molecules. This has an influence on the way that energy is partitioned. Kinetic isotope effects are associated with unidirectional processes like evaporation, dissociation and recombination reactions, as well as biologically mediated enzymatic reactions and diffusion. Like equilibrium isotope effects, kinetic isotope effects include a component related to molecular vibrational frequences, but kinetic isotope effects also include components related to the frequency that the transition state transforms into the products and to the proportionality that relates conversion of transition state to products with conversion of transition state

back to reactants (referred to as commitment to catalysis). The strong dependence of vibrational frequencies and decomposition frequencies on mass yields a relationship between reactions involving more than two isotopes of the same element that is proportional to the isotopic mass difference. These processes are referred to as mass-dependent.

During mass-dependent fractionation processes involving sulfur isotopes, covariation of δ^{34}S, δ^{33}S, and δ^{36}S values have a linear dependence that reflects the relative differences in isotopic masses: fractionations between ^{33}S and ^{32}S, ^{34}S and ^{32}S, and ^{36}S and ^{32}S reflect a 1 amu, 2 amu, and 4 amu mass differences, respectively. Because fractionations depend on vibrational frequences rather than direct mass differences, the relationships between variations δ^{33}S, δ^{34}S, and δ^{36}S values are related to their reduced mass (Hulston and Thode, 1965; Matsuhisa et al., 1978; Young et al., 2002), which are defined as:

$$\lambda = \frac{\frac{1}{m1} - \frac{1}{m2}}{\frac{1}{m1} - \frac{1}{m3}} \tag{1.6}$$

where m1, m2, amd m3 - masses of sulfur isotopes ^{32}S, ^{33}S (or ^{36}S), and ^{34}S respectively, with

$$^{33}\lambda = \frac{\frac{1}{m(^{32}S)} - \frac{1}{m(^{33}S)}}{\frac{1}{m(^{32}S)} - \frac{1}{m(^{34}S)}} \approx 0.515 \tag{1.7}$$

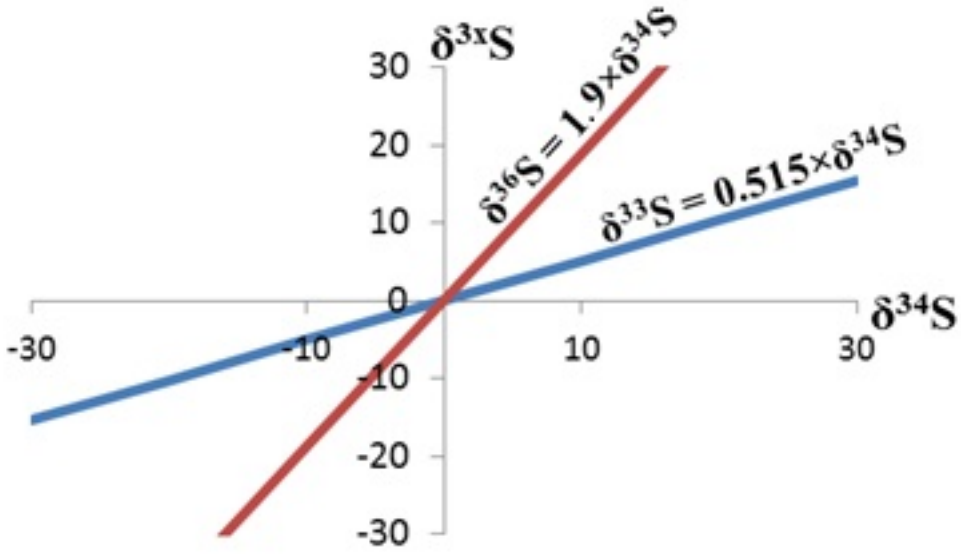

Figure 1.2: Plot represented expected arrays of sulfur isotope data that follow mass-dependent fractionation laws δ^{34}S - δ^{33}S and δ^{34}S vs. δ^{36}S

$$^{36}\lambda = \frac{\frac{1}{m(^{32}S)} - \frac{1}{m(^{36}S)}}{\frac{1}{m(^{32}S)} - \frac{1}{m(^{34}S)}} \approx 1.9 \tag{1.8}$$

On plots of δ^{34}S vs. δ^{33}S and δ^{34}S vs. δ^{36}S in Fig. 1.2 mass-dependent processes are expressed as lines with slopes equal to the factor λ. If the isotopic compositions of natural materials fall off of these lines, mass-independent fractionation (MIF) is considered, which is discussed in the next section.

Fig. 1.3 shows common sources of sulfur and their isotopic composition. The most wide range of δ^{34}S we can see in sedimentary pyrites mediated by biological processes. As in the case of carbon isotopes, enzymes within living organisms prefer to incorporate the lighter ^{32}S isotope during their metabolism.

One of the main natural processes causing mass-dependent fractionation is dissimilatory sulfate reduction by sulfate-reducing bacteria (SRB). In Fig 1.4 a simple

metabolic pathway for sulfate reduction is presented (Rees, 1973).

The total biological fractionation of sulfur isotopes during microbial sulfate reduction reflects the combination of each of these steps. The magnitude of isotopic fractionations produced by sulfate reducers can vary, but may reach δ^{34}S values up to >75‰(Canfield et al., 2010). Fractionation can depend on many factors as has been illustrated in culture experiments, for example:

1. It has been shown that higher rates sulfate reduction are associated with smaller fractionation of sulfur isotopes (Harrison and Thode, 1958);

2. Experiments by Habicht et al. (2002) demonstrated that bacterial sulfate reduction under concentration of SO_4^{2-} less than 200 μM produce small magnitudes of fractionation (generally less than 6‰).

3. It has also been shown that fractionaions decrease with lower temperatures (Harrison and Thode, 1958).

On the other hand, non-biological processes such as evaporation and precipitation of sulfate minerals yield small magnitudes of fractionation, typically around 2‰ (Raab and Spiro, 1991). It is generally agreed that isotopic composition of evaporites represents an isotopic composition of seawater at time of precipitation (Strauss, 2004).

1.5.2 Processes Causing Mass-Independent Fractionation

To quantify deviations from mass-dependent reference lines (see Fig. 1.2) due to mass-independent processes, a capital delta notation (Δ) is used where:

$$\Delta^{3x}S = \delta^{3x}S - \left[\left(1 + \frac{^{34}S}{1000}\right)^{\lambda} - 1\right] \times 1000 \tag{1.9}$$

For the rare isotopes ^{33}S and ^{36}S:

$$\Delta^{33}S = \delta^{33}S - \left[\left(1 + \frac{^{34}S}{1000}\right)^{0.515} - 1\right] \times 1000 \tag{1.10}$$

$$\Delta^{36}S = \delta^{36}S - \left[\left(1 + \frac{^{34}S}{1000}\right)^{1.9} - 1\right] \times 1000 \tag{1.11}$$

After the discovery by Farquhar et al. (2000) of mass-independent fractionation of sulfur isotopes in sedimentary sulfides older than 2.4 Ga, photolysis experiments on sulfur dioxide (SO_2) were conducted to investigate their possible photochmecal origin (Farquhar et al., 2001). Fig. 1.5 illustrates their experimental results.

SO_2 gas was irradiated with light of different wavelengths, and isotopic composition of final products (sulfate and elemental sulfur) was obtained. MIF signal was observed just in the products from the SO_2 photolysis reaction with light of wavelength less than 220 nm. Oxidized products (sulfates) had negative $\Delta^{33}S$ whereas reduced compounds (elemental sulfur) attained positive $\Delta^{33}S$. This is similar to $\Delta^{33}S$ data for geologic samples.

A sharp transition in the magnitude of non-zero $\Delta^{33}S$ signals between rocks

older 2.4 Ga and for those that are younger 2.4 Ga is observed in the geological data set, and this shift has been interpreted to reflect oxidation of the atmosphere resulting in the cessation of MIF preservation in surface environments by ∼2.4 Ga (see Fig. 1.6). After 2.4 Ga small deviations in $\Delta^{33}S$ values have been interpreted to reflect mass-dependent fractionation processes associated with biological cycling of sulfur. For example, Ono et al. (2006) observed a small $\Delta^{33}S$ of up to +0.34‰ from a pyritized Jurassic ammonite. This non-zero $\Delta^{33}S$ value was attributed to a biological process associated with sulfate reduction and with Rayleigh distillation of pore water sulfate that caused a factor λ to shift away from the standard value of 0.515 (Farquhar and Wing, 2003). Measurements of $\Delta^{36}S/\Delta^{33}S$ ratios for Phanerozoic sulfides vary significantly, ranging from -4.4 to -9.8 (with average value -6.9) (Ono et al., 2006), but for Archean sulfides this ratio is very different with a value near -1 (Farquhar et al., 2001). Hence, differences in $\Delta^{36}S/\Delta^{33}S$ ratios have been used to argue for different processes operating in the sulfur cycle at different times in Earth history. Ohmoto et al. (2006) argued different processes of MIF of sulfur isotopes. Notably, measurements of sedimentary rocks deposited between 2.8 and 2.9 Ga demonstrated $\Delta^{33}S$ values near zero in the range of typical MDF signals. This observation maybe interpreted in different ways: 1. oxygen levels fluctuated during the Archean, so MIF signal disappeared at times when oxygen levels exceeded 10^{-5} PAL, or 2. the strength of the MIF signal depends on the volcanic emission rate of the sulfur gases, and photochemical reactions still played an important role in the Archean.

Observation of MIF signal (around -1 to +1‰) from ice core sulfate form-

ing during massive volcanic eruption (Baroni et al., 2007; Savarino et al., 2003) demonstrated that sulfur isotope MIF occurs today above the ozone layer during photooxidation and can be preserved as non-zero $\Delta^{33}S$ and $\Delta^{36}S$ in ice. This process happens over the scale of months to years (Baroni et al., 2007) with the intensity of volcanic eruption causing the range of measured $\Delta^{33}S$ and $\Delta^{36}S$ values.

Differences in volumes and magnetic spins of atoms are another explanation for non-zero $\Delta^{33}S$ values but it does not explain variations in $\Delta^{36}S$ values (see Buchachenko (2013); Oduro et al. (2011)). If photochemical reactions are not the only cause for MIF but thermochemical sulfate reduction caused by magnetic isotope effects (Watanabe et al., 2009) and Raleigh distillation processes also participate, then MIF signals may represent more than oxygen level alone. However, observations for large anomalies in $\Delta^{33}S$ and $\Delta^{36}S$ and $\Delta^{36}S/\Delta^{33}S$ ratio like that observed in pre-2.4 Ga sedimentary pyrite were only found in experiments involving the photolysis of SO_2 (Farquhar et al., 2001). Consequently, for the present, photochemical reactions in an free-oxygen atmosphere remain the main processes thought to cause large $\Delta^{33}S$ anomalies.

1.5.3 Pyrite Formation in Sedimentary Rocks

Because the main source of sulfur in sedimentary rocks is pyrite, mechanisms of its formation should be considered carefully as it can help to resolve problem regarding the preservation of sulfur isotopic signatures. Berner (1970, 1984) considered process of pyrite formation in detail, and identified a number of limiting

factors controlling pyrite formation, including: 1. the rate of sulfate reduction; 2. the availability and reactivity of organic matter; 3. the availability of dissolved sulfate; 4. the amount and reactivity of iron; 5. the rate of sedimentation; and 6. the availability of oxidants.

Direct pyrite formation does not occur in solution because of a high kinetic barriers, but instead the process starts with the formation of iron monosulfides (FeS). Because monosulfide sulfur has oxidation state 2-, there is a need to oxidize sulfur to S^{1-} to form pyrite (Berner, 1970; Schoonen, 2004). There are three mechanisms to form pyrite from monosulfide precusors (i.e. mackinawite) (Schoonen, 2004):

1. FeS conversion via addition of sulfur with sulfur species as an electron acceptor. This mechanism was presented by Berner (Berner, 1970, 1984):

$$FeS + S^0 \longrightarrow FeS_2 \tag{1.12}$$

S^0, elemental sulfur, is an additional sulfur source and electron acceptor (Berner, 1970) and may have a distinct isotopic composition from the sulfur in iron monosulfide. On the basis of series of experiments (Wilkin and Barnes, 1997) with iron monosulfides and multiple sulfur species (zero-valent sulfur S^0, colloidal sulfur, polysulfides S_x^{2-}, hydrogen sulfides (H_2S, HS^{-1}), sulfite SO_3^{2-}, thiosulfite $S_2O_3^{2-}$, and organic sulfur species), it was shown that pyrite is formed in the presence of colloidal elemental sulfur and polysulfides. However, if conditions are slightly oxidizing, pyrite also can be formed with the addition of hydrogen sulfide.

2. FeS conversion via addition of sulfur in form of hydrogen sulfide with a

non-sulfur electron acceptor. Non-sulfur electron acceptor can be O_2, H_2O_2, Fe (III), nitrate, Mn(IV, III), organic carbon and bicarbonate (Berner, 1970; Wilkin and Barnes, 1997);

3. FeS conversion via iron loss, combined with an electron acceptor. Experiments tracing sulfur sources during pyrite formation from FeS and measuring isotopic compositions of reactants and products (Wilkin and Barnes, 1997) demonstrate that sulfur is not added before FeS - pyrite conversion, but Fe^{2+} is released to solution. In slightly oxidizing conditions, a transitional step is the formation of Fe(III) oxyhydroxides near the surface of sulfides (Wilkin and Barnes, 1997). Wilkin and Barnes (1997) proposed that the main mechanism of pyrite formation is iron loss:

$$2FeS + 2H^- \longrightarrow FeS_2 + Fe^{2+} + H_{2(g)} \tag{1.13}$$

However, all above described experiments were conducted in the laboratory and did not include any microbial component. In nature, where processes are inherently more complicated than experiments, bacteria likely play a significant role in pyrite formation using completely different pathways. Pyrite can form framboids and euhedral crystals (Popa et al., 2004). The former occurs during fast rate of pyritization, while the latter occurs when the rate of pyritization is slow (Wilkin and Barnes, 1997).

1.5.4 The Archean Sulfur Cycle

Evidence of mass-independent fractionation of sulfur isotopes (MIF-S) in sulfides and sulfates in rocks older 2.4 Ga (Farquhar et al., 2000) and photolysis experiments of sulfur dioxide (Farquhar et al., 2001) imply the absence of a present day ozone layer in the Earth's atmosphere prior to approximately 2.4 Ga. Because ozone concentrations are directly linked to that of oxygen, the large MIF signals have been used to argue for a low concentration of oxygen in the Archean atmosphere. Using a one-dimensional model, Pavlov and Kasting (2002) demonstrated that MIF-S (as discrete sulfate and elemental sulfur channels) will be efficiently transferred from the atmosphere to Earth's surface when oxygen levels are below 10^{-5} of the present atmospheric level (PAL).

One place in the geological record where we can see a transition from MDF to MIF signals is in the Duitschland Formation in South Africa, which is constrained to be ∼2.32 Ga in age (Bekker et al., 2001, 2004; Guo et al., 2009).

As atmospheric oxygen was very low in the Archean Eon, the rate of oxidative weathering and the flux of sulfur into the ocean and thus sulfate concentration in the ocean is belived to have remained low until the Great Oxidation Event (Farquhar et al., 2000; Guo et al., 2009). The main source of sulfate sulfur at this time is thought to have been associated with photochemistry of other atmospheric sulfur species (such as sulfur dioxide, elemental sulfur, or sulfur monoxide). During photochemical reaction, SO_2 gas, which is thought to come from volcanic emission, would be photochemically transformed into sulfate (SO_4^{2-}) and zero-valent (mainly

elemental S) species (Farquhar et al., 2000).

Quantitative estimation of sulfate concentration in Archean seawater can be made using sulfur isotopic composition of sediments (see Fig. 1.7). It has been noted that before 2.5 Ga sulfur isotopic fractionation is smaller than in younger rocks, and this has been attributed to sulfate reduction under low sulfate concentrations. Habicht et al. (2002) on the basis of experiments defined a threshold of approximately 200 μM for Archean seawater sulfate concentration, although this constraint might also depend on the rate of sulfate diffusion into sediments.

A scheme of the Archean sulfur cycle is shown in Fig. 1.8. Volcanic gases (as either SO_2 or H_2S) initially had zero $\Delta^{33}S$ values. Exposure of gases to UV light results in the photolytic production of two distinct sulfur reservoirs with opposite $\Delta^{33}S$ values. Sulfate from the atmospheric channel with negative $\Delta^{33}S$ values may have been used by sulfate-reducing bacteria (SRB) during dissimilatory processes to produce sulfide, which is preserved in some sedimentary rocks as pyrite with negative $\Delta^{33}S$ compositions. Elemental sulfur from the atmospheric channel with positive $\Delta^{33}S$ values could directly form pyrite as described above. Alternatively, this reduced pool might be oxidized to sulfate through inorganic or biological processes, and then be reduced back to HS^- through bacterial sulfate reduction thereby resulting in the sulfate and elemental sulfur reservoirs mixing.

This study of the Batatal Formation from Brazil is intended to further elucidate the processes of sulfur isotope mass-independent fractionation genesis and preservation in the Neoarchean ocean.

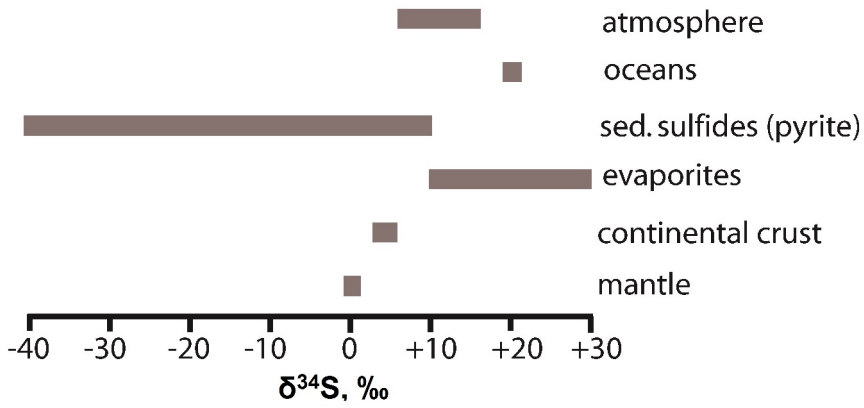

Figure 1.3: Isotopic composition of common sulfur reservoirs. Modified from (McFadden and Kelly, 2011)

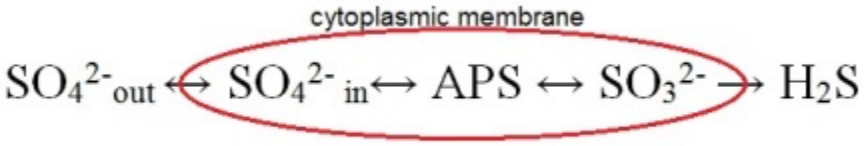

Figure 1.4: A simplified model of metabolic pathways for sulfate reduction proposed by Rees (1973)

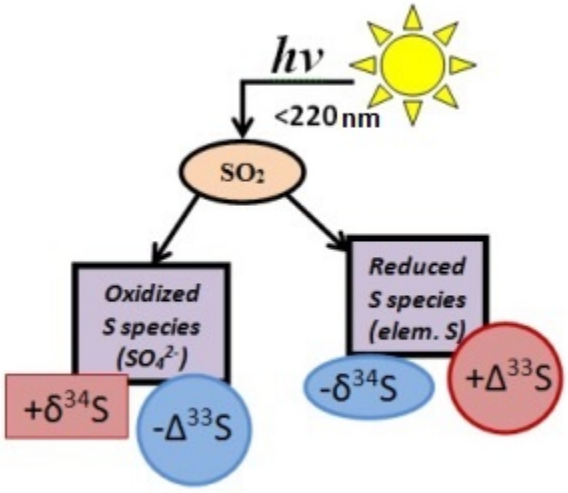

Figure 1.5: A simplified scheme of experiments from Farquhar et al. (2001). SO_2 gas was irradiated with UV light of wavelength ranging from 184.9 to 248 nm. Products of photolysis with less than 220 nm wavelength showed large variations in $\delta^{34}S$ and $\Delta^{33}S$ values. Oxidized species (primary sulfate) had positive $\delta^{34}S$ and negative $\Delta^{33}S$ values while reduced sulfur species (elemental sulfur compounds) had negative $\delta^{34}S$ and positive $\Delta^{33}S$ values.

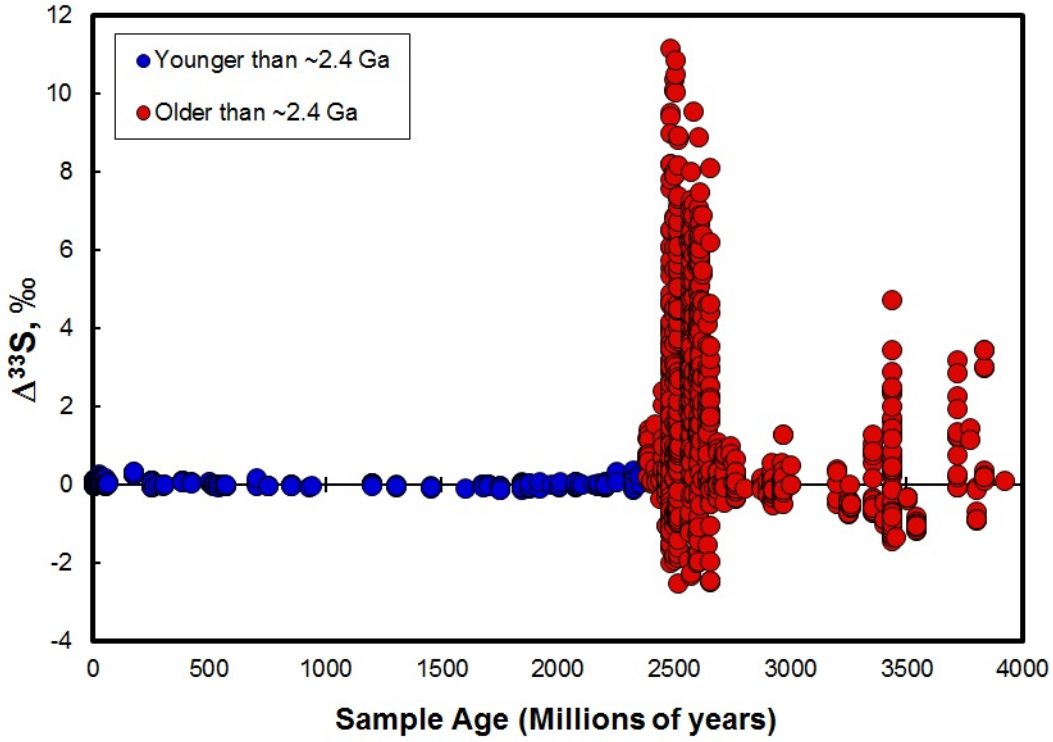

Figure 1.6: Evolution of $\Delta^{33}S$ over geological time. Data is compiled from Bao et al. (2007); Bekker et al. (2004); Cates and Mojzsis (2006); Domagal-Goldman et al. (2008); Farquhar et al. (2000, 2002); Guo et al. (2009); Hu et al. (2003); Johnston et al. (2005, 2006); Kamber and Whitehouse (2007); Kaufman et al. (2007); Kendall et al. (2010); Mojzsis et al. (2003); Ohmoto et al. (2006); Ono et al. (2003, 2006, 2009a); Papineau et al. (2005); Partridge et al. (2008); Philippot et al. (2007); Rouxel et al. (2008); Shen et al. (2009, 2011); Ueno et al. (2008), and Zerkle et al. (2012). Sedimentary rocks older than 2.4 Ga demonstrate non-zero $\Delta^{33}S$ which is attributed to low level of the atmospheric oxygen $< 10^{-5}$ of the present atmospheric level (PAL) (Pavlov and Kasting, 2002). See text for additional details.

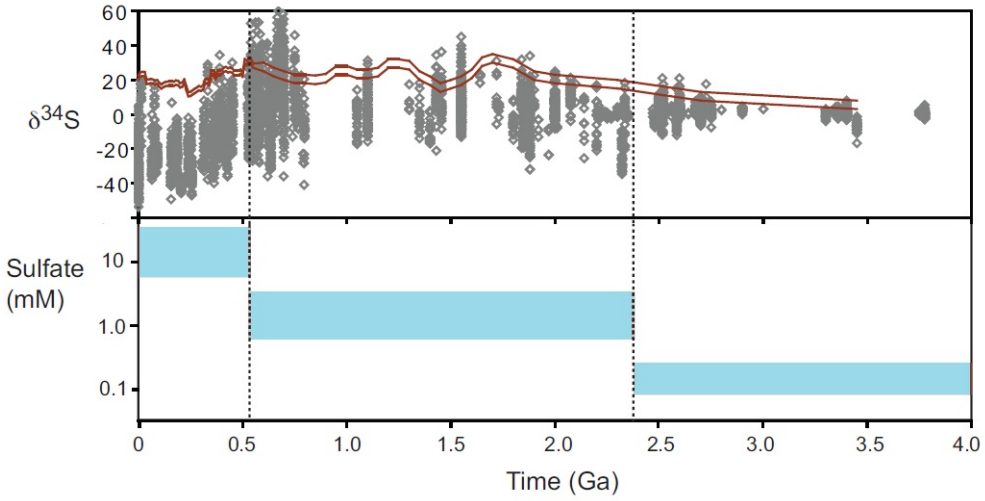

Figure 1.7: Upper plot shows $\delta^{34}S$ of sulfides (grey diamonds) and isotopic composition of seawater (double red line) over time. Lower plot demonstrate ranges SO_4^{2-} concentration in the ocean through geological time: before GOE (2.4 Ga), after GOE (2.4 - 0.542 Ga), Phanerozoic (0.542 Ga - present time). From Canfield and Farquhar (2009)

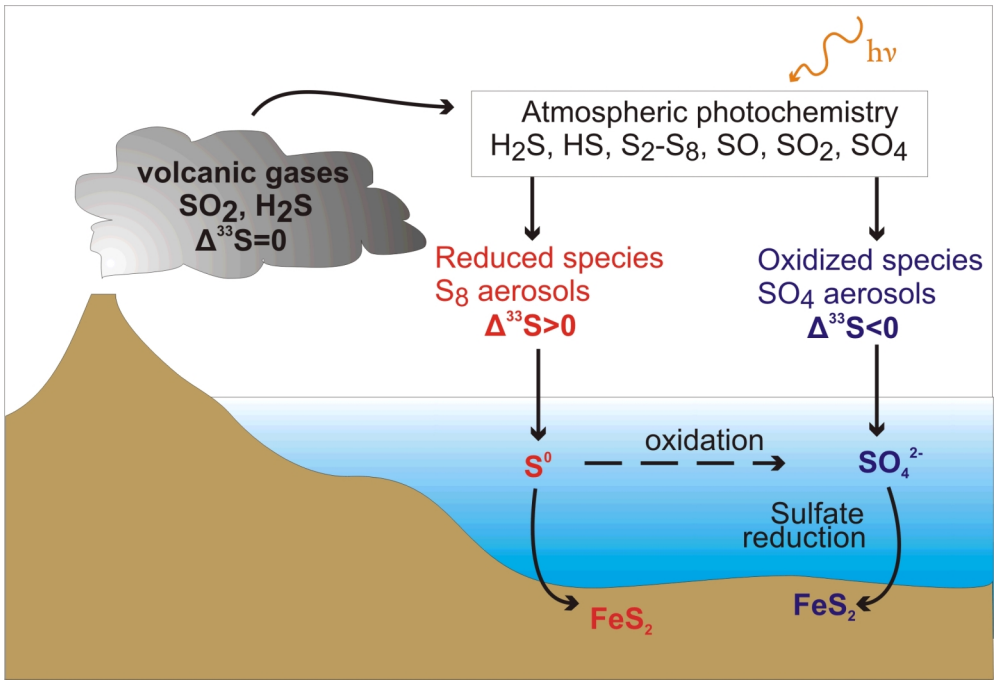

Figure 1.8: Schematic diagram of the Archean sulfur cycle with potential cycles that transfer MIF-S signals to sediments. From (Farquhar and Wing, 2003; Ono et al., 2009a)

Chapter 2

Characteristics of the Batatal Formation

2.1 Geological Settings and Stratigraphy

The Batatal Formation belongs to the Minas Supergroup in south central Brazil near Belo Horizonte (Fig. 2.1). The sedimentary succession comprises three groups: the Caraça, Itabira, and Piracicaba (Bekker et al., 2003) (see Fig. 2.2). The Batatal Formation forms the upper part of the Caraça Group, which overlies the Moeda Formation with a generally sharp contact. Where both formations are thin and the Moeda Formation is argillaceous the contact is gradational. The Batatal Formation is conformable with rocks of the overlying Itabira Group (Dorr, 1969).

The Batatal Formation consists largely of sericitic phyllite and includes minor meta-chert, iron-formation, and graphitic phyllite. Where both the Batatal and Moeda formations are thin and poorly differentiated, the Batatal Formation may also contain significant amounts of quartz. Locally the formation contains significant amounts of chlorite, graphite and carbonaceous material (Dorr, 1969). The Batatal Formation is widespread, but is rarely preserved in outcrops; where it does occur on the surface it is highly weathered.

Fresh samples from the core GDR-117 were collected by Prof. Alan J. Kaufman and graduate student Nick Geboy in 2005 with the assistance of Carlos Noce from Universidade Federal de Minas Gerais. The thickness of the Batatal Formation

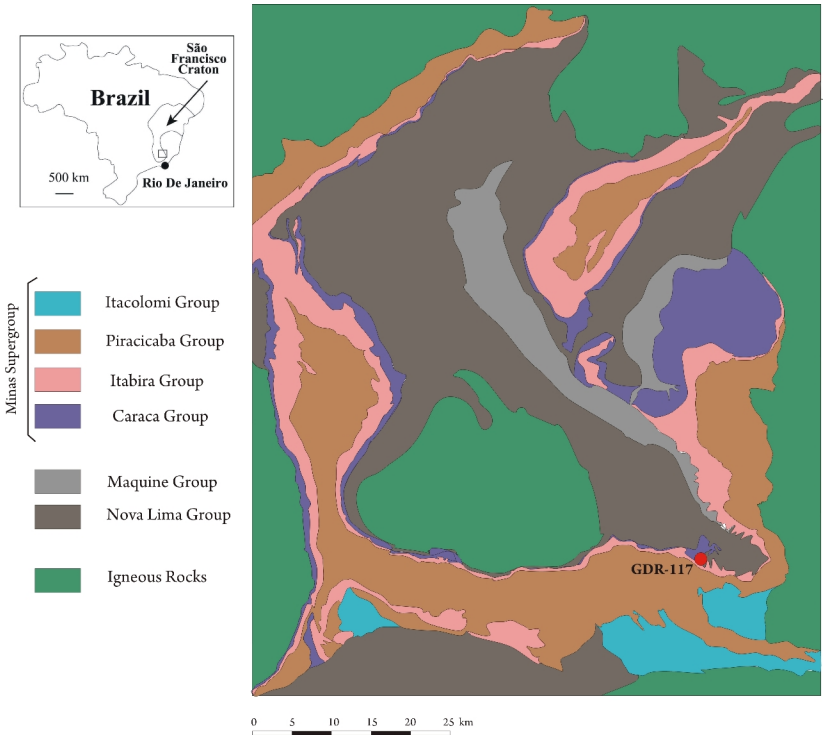

Figure 2.1: Simplified geological map of Iron Quadrangle region with the position of the GDR-117 core. After Dorr (1969)

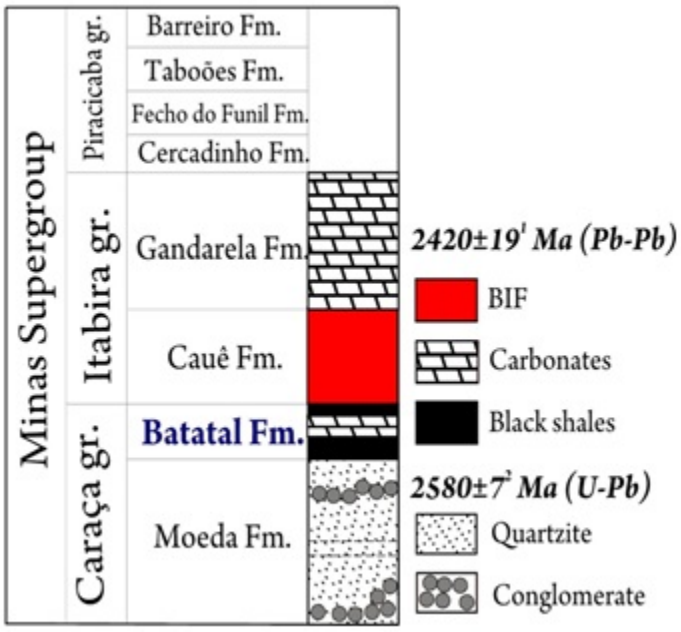

Figure 2.2: Stratigraphy and geochronology of the Minas Supergroup (after Bekker et al. (2003)). 1. age of the Gandarela Formation is from Babinski et al. (1995). 2. age of the upper Moeda Formation is from Hartmann et al. (2006).

ranges from a few meters to more than 200 m (Dorr, 1969). In the GDR-117 core the Batatal Formation consists of upper (38 m) and lower (65 m) black shale intervals sandwiching a thick dolomite (67 m). I divided the GDR-117 core onto three lithostratigraphic subdivisions (see Fig. 2.3). The contact between the lower black shale layer and the carbonate interval is gradational, and between the upper black shale and carbonate (which is brecciated in the upper 10 meters, see Fig. 2.4G) is sharp (see Fig. 2.4F). The brecciation may indicate the effects of exposure, weathering, and karstification of the shallow marine carbonate platform during sea level fall prior to transgression and deposition of the overlying shale facies.

The lower black shale consists of dark grey to black fine-grained mudstone interbedded with coarser grey mudstone in the bottom of the core (Fig.2.4L). Bedding subdivided on the basis of different carbonate content (see Fig.2.4J). In general, the lower black shale interval is homogeneous with locally enrichment in pyrite laminaes and nodules (Fig. 2.4J and K).

Carbonates in the middle of the formation are generally laminated or massive with zones of pyrite enrichment (Fig. 2.4H). In some intervals the carbonates appear stromatolitic (see Fig. 2.4I), but these structures also resemble rolled up microbial mats. Two layers of stromatolitic dolostone were defined (Fig. 2.3). The upper brecciated ten meters of carbonate, close to the upper shale contact, is riddled with chert lenses and veins (see Fig. 2.4G).

The upper shale is generally more enriched in organic matter and pyrite relative to the lower black shale (compare Fig. 2.4E and 2.4J), and between depths of 1240 and 1230 meters is enriched in pyrite nodules, carbonate and quartz (Fig. 2.4B,

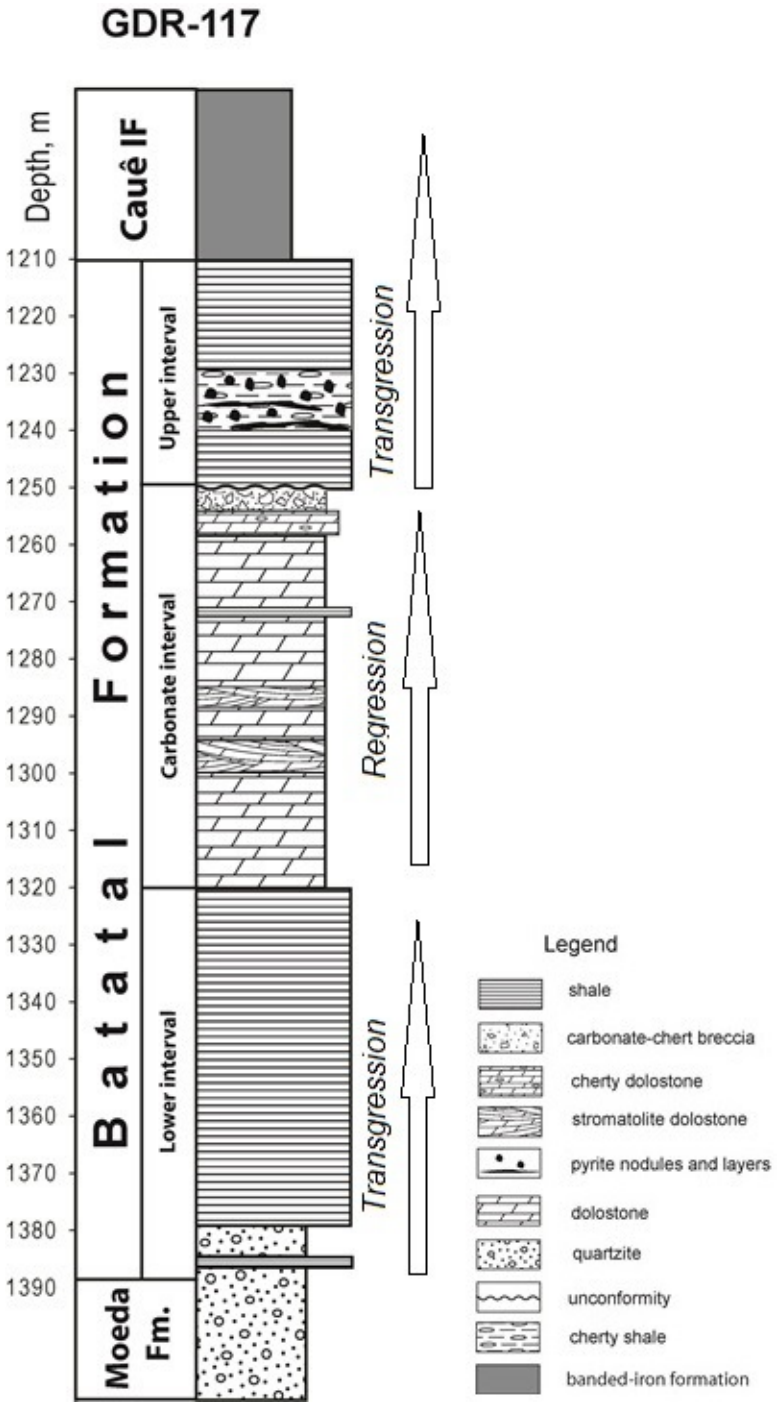

Figure 2.3: Detailed lithology of the core GDR-117. The arrows show stages of transgression/regression.

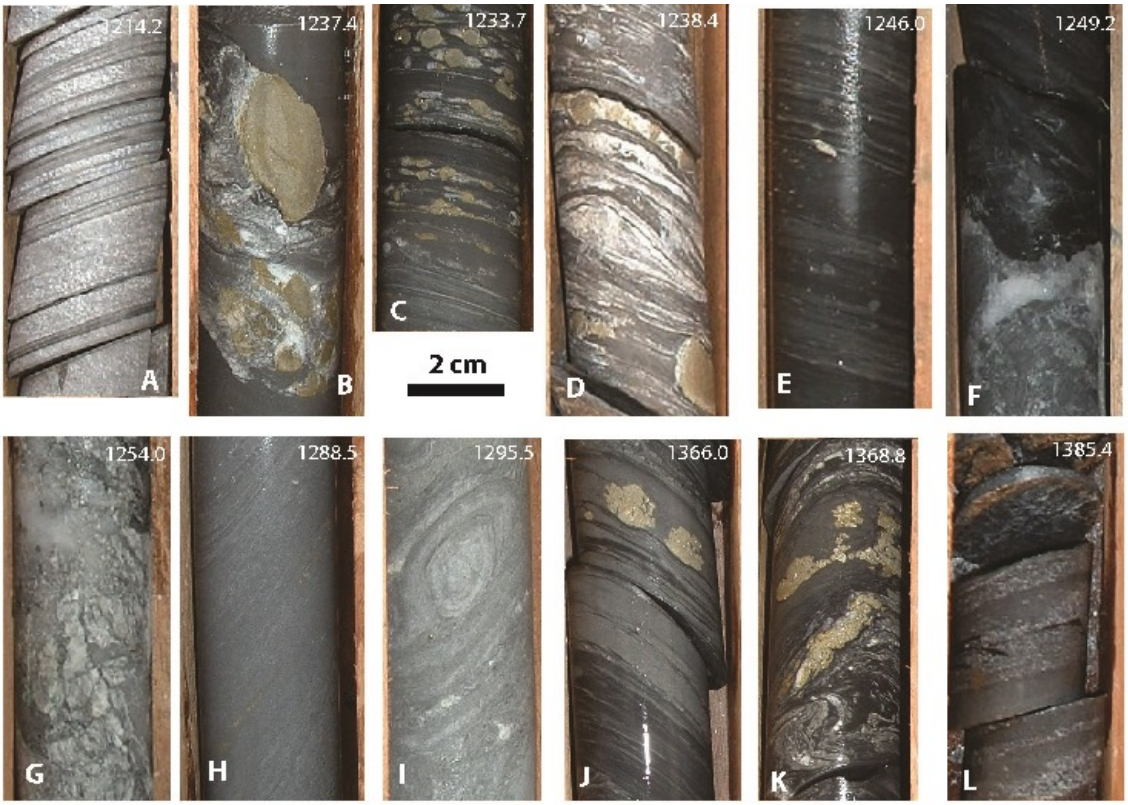

Figure 2.4: Pictures of main lithological types in the GDR-117 core. (A) Shale enriched in silica and carbonate (1214.2 m depth). (B) Detrital pyrite in black shale (1237.4 m depth). (C) Upper shale enriched in organic matter and pyrite nodules (1233.7 m depth). (D) Upper shale enriched in chert, carbonates, and pyrite nodules (1238.4 m depth). (E) Black shale enriched in pyrite (1246.0 m depth). (F) The boundary between carbonate interval and upper black shale (1249.2 m depth). (G) Chert-carbonate breccia (1254.0 m depth). (H) Laminated dolostone with some pyrite laminae (1288.5 m depth). (I) Dolostone with stromatolitic structure (1295.5 m depth) (J) Laminated lower black shales with pyrite nodules (1366.0 m depth) (K) Deformed pyrite veins in shale (1368.8 m depth). (L) Interbedded shale and quartzite (1385.4 m depth)

C, D). Above this interval the upper shale has pyritic laminations in association with quartz-carbonate layers (Fig. 2.4A).

2.2 Geochronology

The age of the upper Moeda Formation quartzite is 2580±7 Ma (detrital zircon, U-Pb SHRIMP), and provides upper limit for the age of the Batatal Formation (Hartmann et al., 2006). The minimum age is constrained by a Pb-Pb carbonate age for the overlying Gandarela Formation of 2420±19 Ma for stromatolitic dolomites (Babinski et al., 1995). These broad constraints indicate that the Batatal Formation was deposited prior to, during or immediately after the Archean-Paleoproterozoic transition at 2500 Ma.

2.3 Interbasinal Correlation of the Batatal Formation

Given available age constraints, it is possible that the contact between the Batatal Formation and the overlying Cauê Iron Formation, might be directly correlated with similarly aged contacts between shale and BIF in South Africa (between the Klein Naute and Kuruman Iron formations), and Western Australia (between the Mt. McRae Shale Formation and the Brockman Iron Formation) (see Fig. 2.5). Rocks in these three successions include black shale, carbonate, chert, and BIF, representing both deep and shallow water marine environments.

The stratigraphic position of the Batatal Formation, however, differs from other two formations insofar as the Brazilian succession was deposited directly on

terrestrial or marginal marine clastic sediments (the Moeda Formation), or basement rocks with a maximum age as far back as >2.61 Ga basement (Bekker et al., 2003). This observation suggests that deposition of the Batatal shale and carbonate coincided with major relative subsidence and transgression over exposed continental rocks. On the other hand, the supposedly equivalent pre-BIF shales in the Campbellrand and Hamersley groups are underlain by thick marine lithologies (see e.g. Cheney (1996)). These geological and geochronological observations suggest that either:

1. The Batatal Formation was formed in a different environment than the other two formations, but from the same open oceanic reservoir (Aspler and Chiarenzelli, 1998). In this case isotopic signature recorded in the Batatal Formation should be similar to those in the Mt. McRae Shale and Klein Naute formations, or

2. The Batatal Formation was deposited in a restricted or stratified marine environment, so the isotopic composition of rocks may differ from other coeval records and record a particular isotopic signature of the Batatal water reservoir, or

3. Deposition of the Batatal Formation was earlier or later than the Mt. McRae Shale and Klein Naute formations, insofar as age constraints provide a wide range of possibilities spanning $\sim$ 150 Ma for the Brazilian deposit. In this situation, the isotopic composition of the Batatal rocks may differ from its comparitors in both time and space, as well as in diagenetic preservation. Information to evaluate these possibilities may be provided by the chemo stratigraphy.

Fig. 2.5 illustrates the suggested correlation of three potentially coincident successions from Brazil, Southern Africa and Western Australia. The main argument

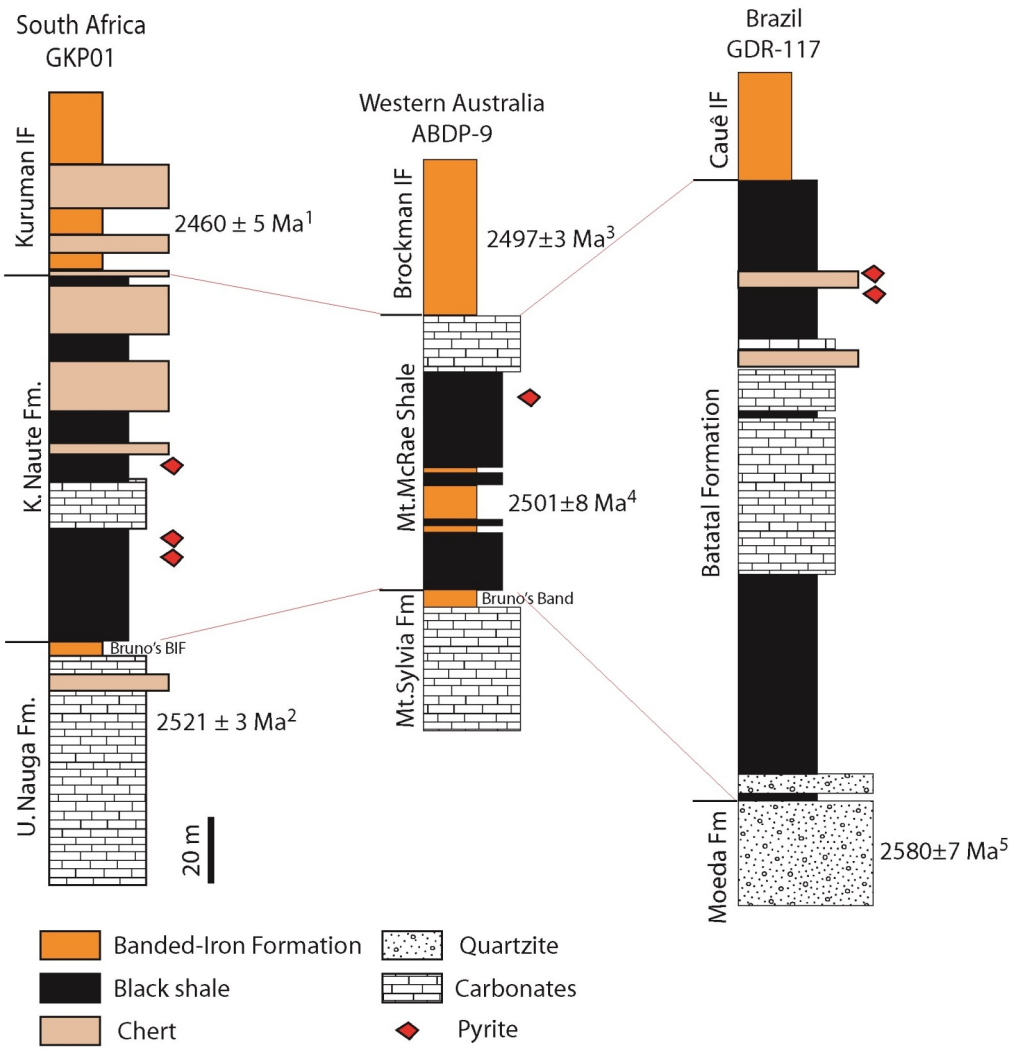

Figure 2.5: Simplified stratigraphic columns of cores GKP01 (South Africa), ABDP-9 (Western Australia), and GDR-117 (Brazil). The scale of each core is the same. As seen the Batatal Formation is thicker and more homogeneous than the Mt. McRae Shale and Klein Naute formations. Pyrite enrichment layers are observed in each core. Lithology is from Dorr (1969); Kaufman et al. (2007); Ono et al. (2009a). Age constraints are from: 1 - Pickard (2003), 2 -Sumner and Bowring (1996), 3 - Nelson et al. (1999), 4 - Anbar et al. (2007), 5 - Hartmann et al. (2006)

about coincidence of these formations is deposition of overlying thick BIF. Notably, thick pyrite enriched layers are also present in all three cores, and it is possible that these pyrite-rich horizons were caused by similar depositional environments or similar source of iron and sulfur to the ocean(s). Time-series isotopic compositions of the Batatal Formation may provide additional clues to the correlation of the three formations.

2.4 Depositional Environments

Depositional environments during accumulation of the Batatal sediments may control preservation of isotopic signatures, so distinguishing the settings in which the rocks were formed is critical to future interpretation.

Black shale

From the beginning of the election study the depositional environments for these rocks have always been speculative (Wignall, 1994). There is no single unifying concept regarding black shale preservation. One of the most famous modern analog of black shale deposition is the Black Sea, where fine silt and clay accumulate at the seafloor in deep and euxinic conditions. However, extending this model to all black shales is unjustified. Contact relationships with surrounding rocks as well as textural preservation is a key to understanding depositional environments.

The lower interval of the Batatal Formation directly overlies the quartzite gravel/conglomerate of the Moeda Formation with a gradational transition (Dorr, 1969). In the GDR-117 core, interbedding between quartzite and shale is observed

in the lower interval (Fig. 2.4L) and is apparent even in thin sections (Fig. 4.1L). Thus, deposition of the lower black shale is inferred to have started on the continental slope in a near shore area where coarse clastic sediments were previously transported. Black shale deposition continued with transgression and deepening of the basin.

The upper shale interval overlies breccia with an unconformity (see Fig. 2.4F) and presents a second transgressive stage associated with the rise of the sealevel. Pyrite concretions, chert-carbonate layers, and high OM content (see Fig. 2.4) may indicate a high-productivity region. The upper interval is similar to that described in Wignall (1994) as maximum flooding black shales with the occurrence of erosional surfaces during sedimentation under a stratified water column.

Carbonates in the middle of the Batatal Formation are usually laminated but occasionally stromatolitic indicating deposition of the carbonate interval in shallow water below the tidal zone. Lamination is highlighted by the presence of thin 1-2 millimeter interbeds of carbonate and silica (see Fig. 4.1G). It has been noticed (Sighinolfi, 1974) that carbonates and silica in Archean might coprecipitate under evaporitic conditions. This could be the case of the Batatal carbonate interval. As will be described below, carbonates have low sulfur content and, subsequently, pyrite abundance. Pyrites usually are associated with silica (see Fig. 4.1H).

Chapter 3

Analytical Methods

This chapter will describe analytical methods used for carbon isotopic analysis (organic and carbonate carbon), carbonate and organic carbon content, sulfur isotopic analysis and petrographic work.

3.1 Sampling

Ninety-one samples in total were collected from the GDR-117 core (28 and 44 samples of upper and lower black shale intervals, respectively, and 18 samples from the carbonate interval). The lithology and description of the core mostly were based on serial photographs taken during the fieldwork in 2005.

For bulk isotopic and elemental analysis samples were crushed by hand using a ceramic mortar and pestle. In case of measuring isotopic composition of pyrite grains, nodules or laminations, they were drilled out using 1-mm drill bit, and powders were collected into glass vials for future analysis.

3.2 Petrographic Observations

Thirty two thin sections, including twenty four shales and eight carbonates, were made by Spectrum Petrographics, Inc. The chips from samples were polished in the Biogeochemistry Laboratory at the University of Maryland to closely observe

ore minerals (particularly pyrite). Observations and photos of thin and polished sections in transmitted and reflected light, respectively, were taken on research Leica petrographic microscope in the Microscope Facility.

3.3 Analysis of Carbonates

3.3.1 Carbonate Weight Percent

To estimate carbonate content, four to five grams of powdered samples were acidified in 50 mL centrifuge tubes with 15 mL of 3M HCl. When effervescence stopped the solutions were centrifuged and decanted, then a new aliquot of acid was added to make sure that all carbonates are quantitatively reacted. Milli-Q-H_2O was then added to the test tubes to purify the samples of the acid. After washing and centrifuging several times, and drying of samples overnight, differences between initial mass of sample and acidified residue were measured to get mass and percentage of carbonate.

3.3.2 Carbonate Carbon and Oxygen Isotopic Composition

The isotopic composition of carbonate was measured using the MultiFlow-IRMS in the Paleoclimate CoLaboratory at the University of Maryland. The reference used for carbon isotopic analysis is JTB-1 ($\delta^{18}O_{PDB}$ = -8.71‰; $\delta^{13}C_{PDB}$= +1.78‰). Exactly 100±10μg of the standard is weighted into exetainers. In the case of samples from the GDR-117 core, an amount of sample is weighed taking into account estimates of carbonate content to match sample peak heights with those of

standards. Ten milliliters of 100% phosphoric acid heated up to ∼90°C is manually added to each exetainer to react with carbonate for one hour and release CO_2. The MultiFlow-IRMS subsequently measures masses 44, 45, and 46 ($^{12}C^{16}O^{16}O$, $^{13}C^{16}O^{16}O$ and $^{12}C^{16}O^{18}O$, respectively). The sample-standard bracketing method is used to account for any drift in the instrument and get precise data and for offset corrections to true values. Uncertainties for $\delta^{13}C_{carb}$ and $\delta^{18}O_{carb}$ are less than 0.1‰ and 0.2‰, respectively.

3.4 Organic Carbon

To measure organic carbon in samples, powders were acidified with 3M HCl as described above. The reference used for organic carbon is urea ($\delta^{13}C_{PDB}$= -29.39‰, wt%C_{org}=20%). Exactly 100±10μg of standard is placed in a tin cup. Because samples have much less organic matter than the standard, about 1000μg of pre-acidified samples is weighted into tin cups. The samples are combusted to convert organic carbon to CO_2. Masses of 44 and 45 ($^{12}C^{16}O^{16}O$ and $^{13}C^{16}O^{16}O$, respectively) are measured with the MultiFlow-IRMS in the same laboratory to obtain $\delta^{13}C_{org}$ values. Organic matter content is determined by comparison of standard and sample peak heights, and these are calculated for the whole rock based on quantified carbonate loss. Uncertainties for $\delta^{13}C_{org}$ and organic carbon content are < 0.1‰ and < 2%, respectively. Further calculation procedure of C_{org} content in rocks from acidified samples takes place.

3.5 Sulfur Isotope Measurements

Sulfur isotopes were measured in bulk rocks and in pyrite segregations (nodules, laminaes, enriched layers). To measure sulfur isotopic composition of nodules and other pyrite segregations, a drilling technique was used. Before drilling, rock chips were polished and washed with ethanol. Each drilling spot was mapped on the pictures scanned for each polished sample (see Fig. 3.1).

Due to the low abundance of sulfur in shale samples from the Batatal core (generally less than 0.1 wt.% S), two to five grams of rock powder were used for the Chrome-Reducible Sulfur (CRS) extractions. In the case of drilled pyrite, less than 0.5 g is utilized for the extraction. For whole rocks, the method applied is described in Canfield et al. (1986) where hot 5M HCl is used to liberate acid volatile sulfur (AVS) and subsequently Cr(II) reduction solution is used to extract sulfur from pyrite and other disulfides. These procedures release hydrogen sulfide gas, which is trapped in 0.3M $AgNO_3$ solution, where sulfide reacts with silver ions to form Ag_2S. The apparatus for this procedure is illustrated in Fig. 3.2. After precipitation of silver sulfide the samples are aged for one week in the dark to allow for silver metal and silver hydroxide contaminants to dissolve into the nitrate solution. The silver sulfide samples were then filtered, washed with 1M NH_4OH and ultrapure Milli-Q water, and then dried at 50°C overnight.

Silver sulfide samples of 0.1 mg were weighed into tin cups with a strong oxidizer V_2O_5 for analysis using a Eurovector EA coupled to an Isoprime-IRMS. During EA-IRMS analyses, silver sulfides are oxidized to SO_2 and ratios of masses $^{32}SO_2$

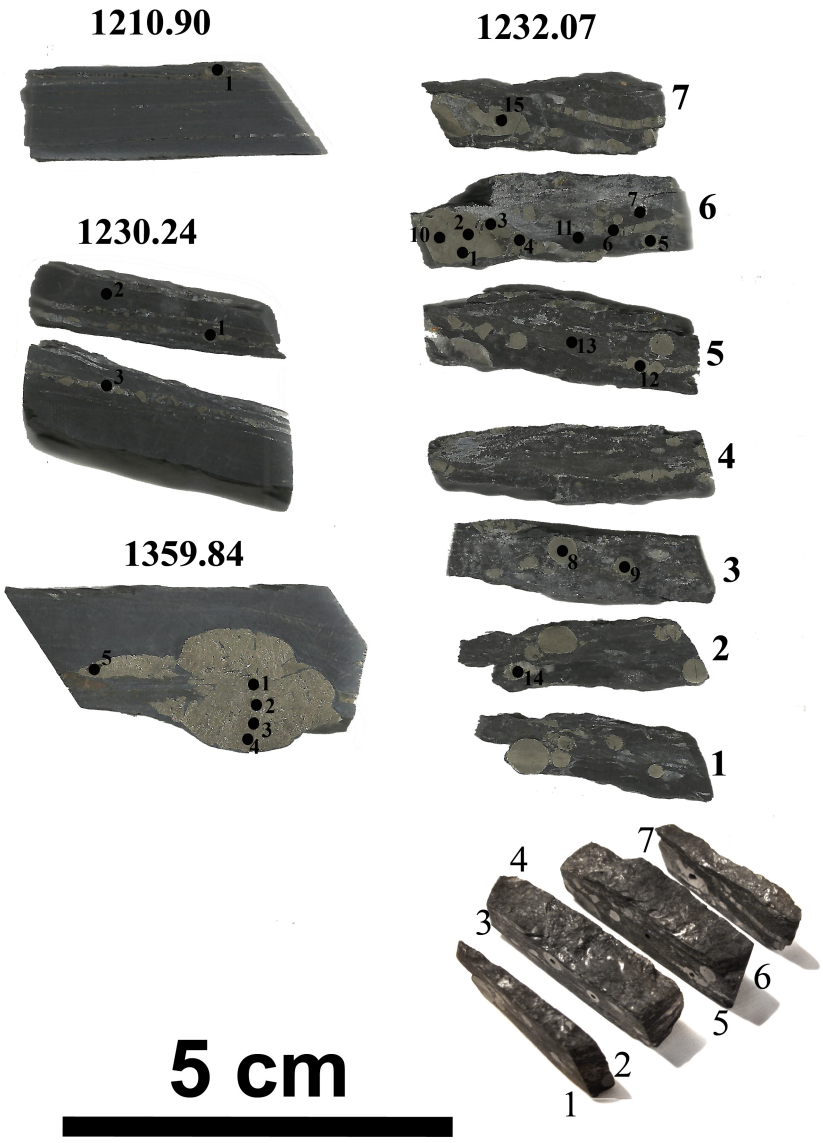

Figure 3.1: Photographs of drill-core samples with mapped drilled spots for sulfur isotopic analysis. The size of the drill bit is about 1 mm.

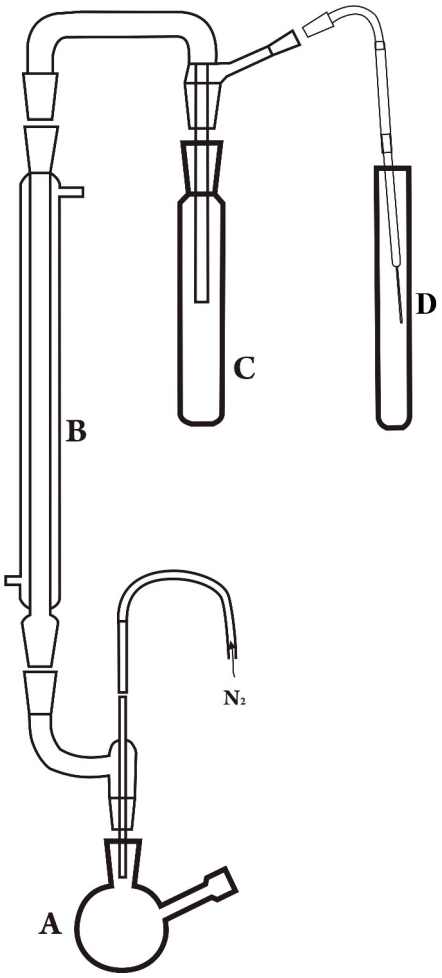

Figure 3.2: Apparatus for the chromium-reducible sulfur procedure. A sample is placed in the boiling flask (A) with 5M HCl and acidic $CrCI_2$ solution, and heated up to 80°C for 3.5 hours. The H_2S gas is released and moves up through the condenser (B), then is bubbled through the tube (C), and is trapped in a $AgNO_3$ solution, forming Ag_2S precipitate(D)

and $^{34}SO2$ are measured to yield $\delta^{34}S$ values with uncertainties less than 0.3‰. Sulfur isotopic compositions are represented as delta notation (δ), a measure of the ratio of a minor isotope to a major isotope in a sample relative to that in a standard material, CDT (Canyon Diablo Troilite).

Silver sulfide samples of two to three mg were weighed and sealed in aluminum capsules for fluorination analyses and isotope ratio of SF_6 using a ThermoFinnigan MAT 253. The production of SF_6 from silver sulfide precipitates is completed by loading the samples in aluminum foil packets into Ni bombs with fluorine gas and heating to 250°C overnight. The SF_6 gas is purified through several steps of cryogenic separation, passivation, and gas-chromatographic purification. Purified SF_6 is loaded into the bellows of the mass-spectrometer, where the isotopic ratios are determined by the intensity of SF_5^+ ion beams at masses 127, 128, 129, and 131. The ThermoFinnigan MAT 253 measurements have estimated uncertainties of 0.14, 0.008, and 0.2‰(1σ) for $\delta^{34}S$, $\Delta^{33}S$, and $\Delta^{36}S$, respectively.

Chapter 4

Results

4.1 Petrography

In the following sections, mineral and textutal characteristics of black shales and carbonates are described. Photomicrographs of thin and polished sections are provided for each of three intervals of the Batatal Formation (subdivision see on Fig. 2.3).

Lower Shale Interval

The main structure of the black shales are thin bedding controlled by rhythmical alternation of beds (thickness from a few millimeters to tens of centimeters) variably enriched in organic matter, carbonates, and silicates (mainly chert). Near the boundary with the Moeda Formation black shale and quartzite are interbedded (see Fig. 4.1L). Slightly higher in the lower shale interval the sedimentary rocks are rich in round quartz grains, which disappear upsection likely associated with marine transgression and inland migration of the shoreline. Otherwise, the texture of the lower black shale interval is homogeneous and thinly-laminated (see Fig. 4.1J and K).

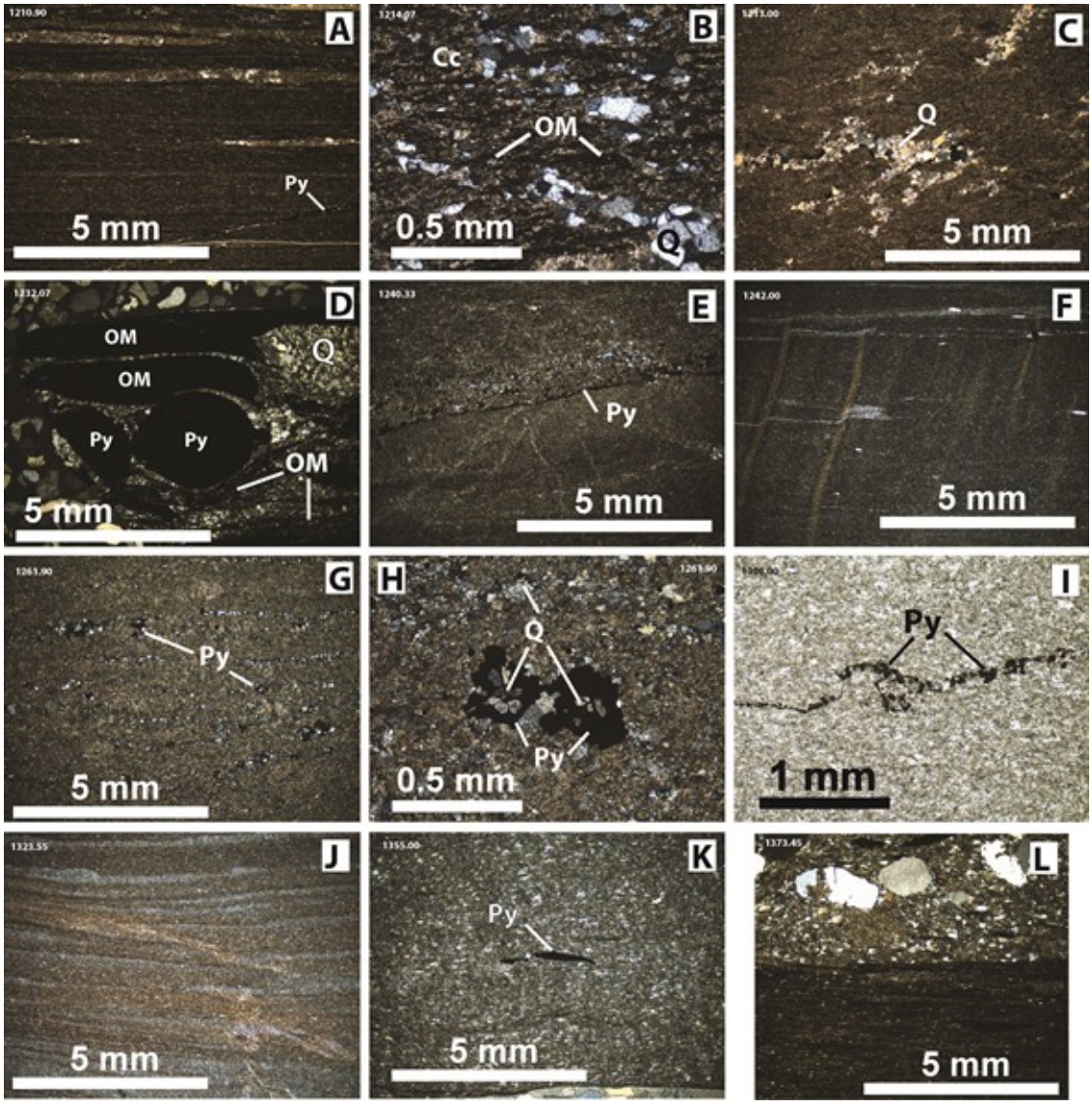
A
Py
5 mm
B
Cc
OM
0.5 mm
Q
C
Q
5 mm
D
OM
OM
Q
Py
Py
OM
5 mm
E
Py
5 mm
F
5 mm
G
Py
5 mm
H
Q
Py
0.5 mm
I
Py
1 mm
J
5 mm
K
Py
5 mm
L
5 mm

Pyrite in the lower black shales is rarely observed. Locally, pyrite forms large diagenetic nodules up to two cm, and irregularly-shaped veins rich in pyrite and chert (Fig. 2.4J) also occur. The source of the pyrite veins is likely hydrothermal. In polished section, visible pyrite is rare. The matrix is poor in pyrite grains except in some parts where pyrite (maximum size of grains less the 0.1 mm) is associated with quartz (see Fig. 4.2O).

Upper Shale Interval

The upper shale has complex structures and textures. The upper black shales are enriched in silica in the form of veins (Fig. 2.4C), beds (Fig. 4.1A), and randomly shaped segregations (Fig. 4.1C). Silicification is thought to be a secondary process, occurring after sediment consolidation. However, close relationships with pyrite suggest that silica also played a role during pyrite formation. The content of organic matter and carbonate minerals is higher in the upper interval (see. e.g.

Figure 4.1 ***(preceding page)*****:** Microphotographs of thin sections from each interval in the GDR-117 core. **The upper interval**: (A) sample GDR-1210.90 in cross-polarized light with 1.5X magnification. Q-Cc laminaes and Py vein in black shale (B) sample GDR-1214.07 in X nicol, 10X. Shale enriched in silica, carbonate, and OM (C) sample GDR-1213.10 in X nicol, 1.5X. Shale with quartz (D) sample GDR-1232.07 in X nicol, 1.5X. Shale enriched in OM and pyrite nodules encrusting with quartz (E) sample GDR-1240.33 in X nicol, 1.5X. Shale subsurface or biofilm enriched in pyrite (F) sample GDR-1242.00 in X nicol, 1.5X. Shale with lamination and diagenetic deformation; **The carbonate interval**:(G) sample GDR-1261.90 in X nicol, 1.5X. Laminated dolostone with silica layers associated with pyrite (H) sample GDR-1261.90 in X nicol, 10X. Pyrite associated with quartz in dolostone (I) sample GDR-1308.00 in || nicol, 5X. Py and OM formed biofilm; **The lower interval**: (J) sample GDR-1323.55 in X nicol, 1.5X. Lamination in fine-grained shale (K) sample GDR-1355.00 in X nicol, 1.5X. Shale with pyrite (L) sample GDR-1373.45 in X nicol, 1.5X. Boundary between black shale and clastic sand.

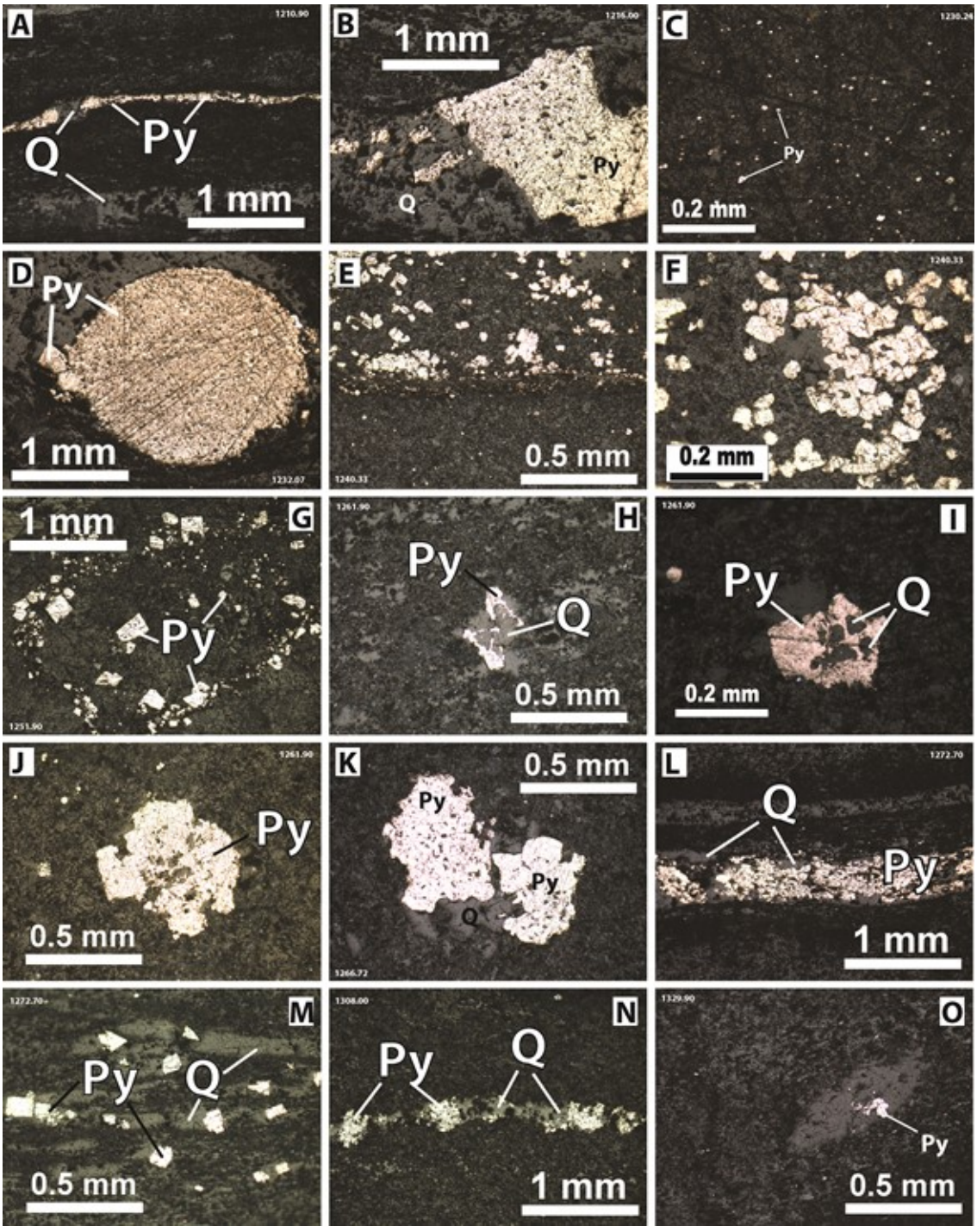
A
1210.90
Q
Py
1 mm
B
1 mm
Py
Q
C
1230.24
Py
0.2 mm
D
Py
1 mm
1232.07
E
0.5 mm
1240.33
F
1240.33
0.2 mm
1 mm
G
Py
1251.90
H
1261.90
Py
Q
0.5 mm
I
1261.90
Py
Q
0.2 mm
J
1261.90
Py
0.5 mm
K
0.5 mm
Py
Py
Q
1266.72
L
1272.70
Q
Py
1 mm
M
1272.70
Py
Q
0.5 mm
N
1308.00
Py
Q
1 mm
O
1329.90
Py
0.5 mm

Fig. 4.1B and 4.2A). At the bottom of this interval shales are more fine-grained with small post-depositional deformation (Fig. 4.1F).

In most of the rocks pyrite is disseminated with grain size less than 0.05 mm. Pyrite also forms enriched layers (Fig. 4.1E and 4.2E) with small grains ∼0.1 mm, nodules (Fig. 4.2D), veins (Fig. 4.1A), and laminations (Fig. 4.2A). Sometimes framboid-like shape grains are observed (Fig. 4.2F). Secondary recrystallized pyrite is observed around pyrite nodules as euhedral crystals (see Fig. 4.2D)

Carbonate Interval

Most of the carbonates rocks are thinly-laminated. In some parts of the carbonates, a stromatolitic structure is observed, but these may also be interpreted as remnants of rolled up microbial mats that accumulated after a storm event. Laminations are present as interbedded thin layers of silica and dolomite (see Fig. 4.1G). Pyrite grains are often associated with organic matter and silica (Fig. 4.2N and Fig. 4.1I). Pyrite in carbonates usually occurs as irregular euhedral-like grains. In the

---

Figure 4.2 ***(preceding page)*****:** Microphotographs of pyrite polished sections in reflected light from each interval in the GDR-117 core. **The upper interval**: (A) sample GDR-1210.90 with 5X magnification. Pyrite laminae with silica (B) sample GDR-1216.00, 5X. Pyrite nodule with silica (C) sample GDR-1230.24 , 20X. Dissemiated pyrite in shale (D) sample GDR-1232.07 , 5X. Pyrite nodule incrusting with silica. To the left of the nodule later euhedral pyrite is observed (E) sample GDR-1240.33 , 10X. Subsurface in shale enriched in pyrite (F) sample GDR-1240.33 ,20X. Framboid-lika shape of pyrite grains; **The carbonate interval**:(G) sample GDR-1251.90, 5X. Pyrite euhedral grains in breccia (H) sample GDR-1261.90, 10X. Pyrite associated with quartz (I) sample GDR-1261.90, 20X. Pyrite euhedral crystal with quartz (J) sample GDR-1261.90, 5X. Pyrite euhedral crystal (K) sample GDR-1266.72, 5X. Pyrite grains associated with silica (L) sample GDR-1272.70, 5X. Pyrite laminae associated with silica in OM-rich shale inside the carbonate interval (M) sample GDR-1272.70, 10X. Disseminated pyrite grains associated with silica (N) sample GDR-1308.00, 5X. Pyrite-quartz laminae; **The lower interval**: (O) sample GDR-1329.90 , 10X. Pyrite grain in silica

sample GDR-1261.90 different generations of diagenetic pyrite are observed. In Fig. 4.2H pyrite forms grain facets around quartz. Fig. 4.2I illustrates pyrite growing to a euhedral shape. Quartz is observed within the pyrite grains (Fig. 4.1H). This process ends with formation of pyrite grains seen in Fig. 4.2J and K. The formation of pyrite in this pathway is thought to occur due to low organic matter content, low iron or/and sulfur availability, or a depositional rate. Pyrite-rich laminations are also observed in the dolostone samples (Fig. 2.4G and 4.2N)

In the layer of black shale inside the dolomite interval ($\sim$ 1272 m depth) pyrite occurs in the matrix as euhedral grains $\sim$ 0.1 mm size associated with silica (Fig. 4.2M). This pyrite is thought to have formed during diagenesis of sediments accumulating at a rapid rate. Breccia that formed after carbonate deposition contains a large amount of silica and recrystallized carbonate minerals (see Fig. 2.4F). Euhedral pyrite here is detrital (Fig. 4.2G).

4.2 Carbon and Oxygen Data

The concentration and isotopic composition of organic carbon and carbonate carbon and oxygen isotopic data are presented in Table. 4.1. The carbonate content of samples is variable (4.3). Lower black shales have much less carbonate content than those in the upper shale interval, with an average of 17($\pm$20) wt.% and 50($\pm$30) wt.%, respectively. Carbonate rocks have an average 79($\pm$8) wt.% of carbonates except the sample GDR-1727.70 from a black shale layer with $\sim$2 wt.% of $CaCO_3$. Figure 4.3 demonstrates carbonate concentration against stratigraphic

height.

In **the lower interval** carbonate content increases from almost no carbonate at the lower boundary to more than 50% near the upper boundary. This trend is probably related to transgression of the ocean and increasing sealevel. Carbon isotopic composition of carbonate in the lower shale shows increasing $\delta^{13}C_{carb}$ values from -9‰ to -5.3‰ upwards the core.

In **the carbonate interval**, rocks have a uniform carbonate content of about 80%. The $\delta^{13}C_{carb}$ values here are uniform throughout almost the whole interval and vary between -0.1 to -0.7‰, with the most negative value at the base with a $\delta^{13}C_{carb}$ value of -2.9‰. Such values close to zero are similar to the carbon isotopic composition of modern seawater, and also similar to broadly correlative shallow water Neoarchean carbonates worldwide.

The upper black shale interval is characterized by more variable carbonate concentration and a heavier carbon isotopic composition than the lower shale interval. Such variable carbonate content is attributed to secondary alteration. $\delta^{13}C_{carb}$ values fluctuate between -7.3 and -0.8‰. Most negative $\delta^{13}C_{carb}$ value (-7.3‰) is observed in pyrite-rich interval. Higher in the core, shale carbonate becomes more enriched in ^{13}C.

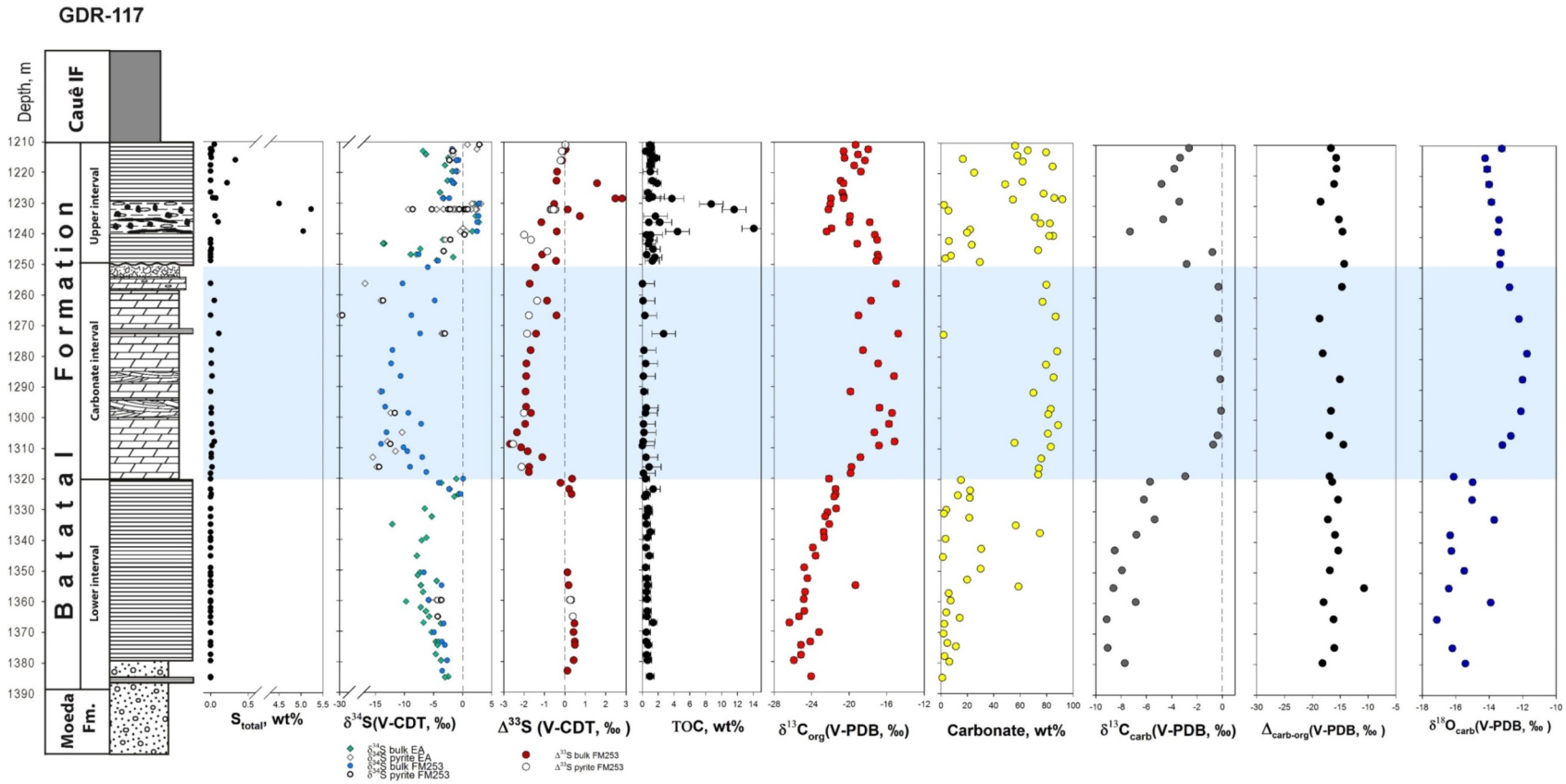

Figure 4.3: Plot of sulfur (wt.%Stotal, $\delta^{34}S$, and $\Delta^{33}S$), carbon (wt.%TOC, carbonate content, $\delta^{13}C_{org}$, and $\delta^{13}C_{carb}$), and oxygen ($\delta^{18}O_{carb}$) data against stratigraphic position in the core GDR-117. Legend for stratigraphy see on Fig. 2.3. Uncertanties are presented in the Table 4.1

In terms of oxygen isotopic composition, the Batatal Formation can be divided into two zones: the lower shale interval with most negative and variable $\delta^{18}O_{carb}$ values, and carbonate and upper shale intervals with less variable $\delta^{18}O_{carb}$ values.

In the lower interval $\delta^{18}O_{carb}$ values vary from -17.1 to -13.7‰. Oxygen isotopes appear to co-vary with carbon isotopes. The carbonate interval is characterized by a low range in $\delta^{18}O_{carb}$ values between -13.2 and -11.8‰. The most negative $\delta^{18}O_{carb}$ value equal to -16.1‰was measured near the boundary with the lower shale interval. Trend of $\delta^{18}O_{carb}$ continues to the upper interval where values vary from -14.3 to -13.3‰.

The coupled relationship between $\delta^{13}C_{carb}$ and $\delta^{18}O_{carb}$ in each interval is demonstrated in Fig.4.4. A positive correlation is observed in the lower shale interval. Data from the carbonate and upper shale intervals show conservative behavior of $\delta^{13}C_{carb}$ and $\delta^{18}O_{carb}$, respectively.

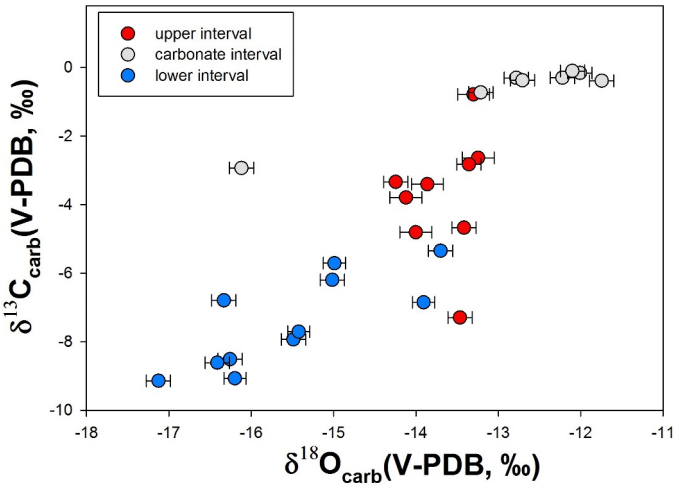

Figure 4.4: Plot of $\delta^{13}C_{carb}$ vs. $\delta^{18}O_{carb}$ in the GDR-117 core for three intervals

4.2.1 Organic carbon

Total organic carbon in the first two intervals of the GDR-117 core have an average concentration less than 1%. On the other hand, in the upper black shale average organic carbon content achieves 2-3% with a maximum concentration of 14.06% in the sample GDR-1238.25. In this interval organic matter burial (or preservation) rate was either much higher. Figure 4.3 shows TOC and $\delta^{13}C_{org}$ variations according to stratigraphy. From the bottom moving upwards into the lower black shale interval $\delta^{13}C_{org}$ values increase from ∼-26‰ to -22‰. The carbon isotopic composition of carbonate preserves a trend of ^{12}C depletion with average $\delta^{13}C_{org}$ value -17(±2) ‰. In contrast, the upper black shales have carbon isotopic composition depleted in ^{12}C. From the breccia-lower interval boundary upwards, $\delta^{13}C_{org}$ decreases, and an average value is approximately -20(±2)‰. The pyrite-rich interval has more negative values of $\delta^{13}C_{org}$ along with elevated TOC (see Fig. 4.3).

The cross-plot on the Fig. 4.5 shows a correlation between wt.% carbonate - $\delta^{13}C_{org}$: the more weight percent of carbonate the more enriched isotopic composition in ^{13}C. A positive correlation was observed between the carbon isotopic composition of organic matter and of carbonate in rocks (Fig. 4.6).

The most striking feature about the carbon isotopic compositions of the Batatal Formation rocks is the consistent and low fractionation between them in all three intervals. $\Delta_{C_{org}-C_{carb}}$ varies from 12.9 to 18.7‰ with average value ∼15‰ (see Fig. 4.3).

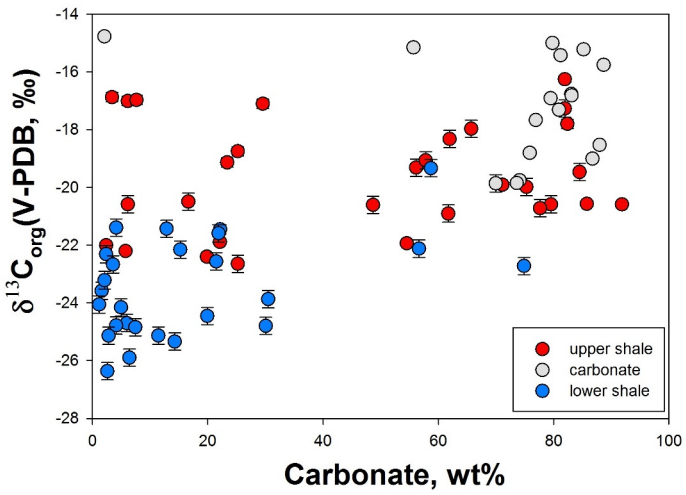

Figure 4.5: Plot of carbonate content - $\delta^{13}C_{org}$ in the GDR-117 core for three intervals

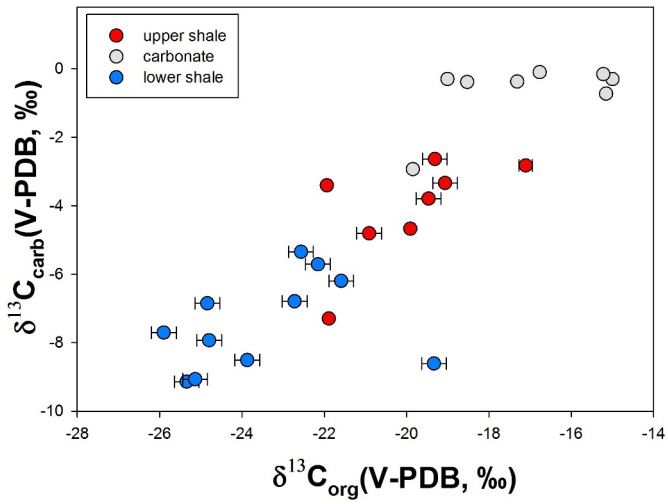

Figure 4.6: Plot of $\delta^{13}C_{org}$ vs. $\delta^{13}C_{carb}$ in the GDR-117 core for three intervals

Table 4.1: Organic carbon and carbonate abundances (wt.%) and isotope results ($\delta^{13}C_{org}$, $\delta^{13}C_{carb}$)

Samples	$\delta^{13}C_{org}$	$\pm\sigma$	$wt.\%C_{org}$	$\pm\sigma$	$wt.\%Carb$	$\delta^{13}C_{carb}$	$\pm\sigma$	$\delta^{18}O_{carb}$	$\pm\sigma$
1210.90	-19.31	0.30	0.99	0.52	56.14	-13.25	0.20	-2.64	0.05
1212.38	-17.97	0.30	1.08	0.52	65.71				
1213.00	-20.59	0.30	0.43	0.52	79.55				
1214.07	-19.07	0.30	1.12	0.52	57.80	-14.25	0.20	-3.34	0.05
1215.20	-20.50	0.30	1.73	0.52	16.63				
1216.00	-18.32	0.30	1.17	0.52	61.96				
1217.66	-19.47	0.30	1.05	0.52	84.50	-14.12	0.20	-3.79	0.05
1219.65	-18.75	0.30	0.93	0.72	25.22				
1222.65	-20.91	0.30	1.25	0.52	61.72	-14.00	0.20	-4.81	0.05
1223.46	-20.61	0.30	1.89	0.52	48.67				
1226.53	-20.72	0.30	0.72	0.52	77.67				
1227.90	-20.57	0.30	1.29	1.47	85.77				
1228.35	-20.59	0.30	0.85	1.47	91.88				
1228.45	-21.94	0.30	3.74	1.47	54.53	-13.86	0.20	-3.41	0.05
1230.24	-22.01	0.30	8.70	1.47	2.38				
1232.07	-22.21	0.30	11.58	1.47	5.75				
1234.25	-19.91	0.30	1.66	1.47	71.14	-13.42	0.20	-4.67	0.05
1236.25	-19.99	0.30	0.97	0.52	75.29				
1236.26	-17.80	0.30	0.84	0.72	82.39				
1238.25	-21.89	0.30	14.06	1.47	22.12	-13.47	0.20	-7.30	0.05
1239.27	-22.40	0.30	4.45	1.47	19.85				
1240.33	-17.27	0.30	0.67	0.52	81.96				
1242.00	-17.01	0.30	0.95	0.72	6.13				
1243.26	-19.14	0.30	0.78	0.72	23.37				
1245.00			1.36	0.72	73.54	-13.30	0.20	-0.79	0.05

Continued on next page

Table 4.1 – continued from previous page

Samples	$\delta^{13}C_{org}$	$\pm\sigma$	$wt.\%C_{org}$	$\pm\sigma$	$wt.\%Carb$	$\delta^{13}C_{carb}$	$\pm\sigma$	$\delta^{18}O_{carb}$	$\pm\sigma$
1246.81	-16.97	0.30	0.56	0.72	7.64				
1247.70	-16.88	0.30	1.59	0.72	3.39				
1248.88	-17.11	0.30	1.27	0.72	29.54	-13.36	0.20	-2.83	0.05
1256.33	-15.00	0.30	0.03	1.47	79.80	-12.78	0.20	-0.31	0.05
1261.90	-17.67	0.30	0.09	1.47	76.91				
1266.72	-19.01	0.30	0.33	1.47	86.74	-12.22	0.20	-0.30	0.05
1272.70	-14.78	0.30	2.70	1.47	2.07				
1278.10	-18.53	0.30	0.21	1.47	87.98	-11.75	0.20	-0.39	0.05
1282.47	-16.91	0.30	0.43	1.47	79.48				
1286.60	-15.22	0.30	0.14	1.47	85.21	-12.01	0.20	-0.16	0.05
1291.65	-19.86	0.30	0.20	0.52	69.97				
1296.94	-16.77	0.30	0.51	1.47	83.07	-12.10	0.20	-0.10	0.05
1298.65	-15.43	0.30	0.40	1.47	81.21				
1302.23	-15.76	0.30	0.15	1.47	88.68				
1305.00	-17.32	0.30	0.22	1.47	80.93	-12.71	0.20	-0.38	0.05
1308.00	-15.15	0.30	0.12	1.47	55.69	-13.21	0.20	-0.73	0.05
1309.91	-16.82	0.30	0.02	1.47	83.13				
1313.13	-18.81	0.30	0.46	1.47	75.88				
1316.30	-19.75	0.30	0.86	1.47	74.08				
1318.37	-19.85	0.30	0.15	1.47	73.60	-16.12	0.20	-2.93	0.05
1320.17	-22.15	0.30	0.41	0.52	15.24	-14.99	0.20	-5.71	0.05
1323.55	-21.45	0.30	1.37	0.72	22.15				
1325.20	-21.44	0.30	0.55	0.52	12.85				
1326.00	-21.59	0.30	0.32	0.52	21.87	-15.02	0.20	-6.20	0.05
1329.90	-21.39	0.30	0.75	0.52	4.12				
1331.14	-22.31	0.30	0.77	0.52	2.35				

Continued on next page

Table 4.1 – continued from previous page

Samples	$\delta^{13}C_{org}$	$\pm\sigma$	$wt.\%C_{org}$	$\pm\sigma$	$wt.\%Carb$	$\delta^{13}C_{carb}$	$\pm\sigma$	$\delta^{18}O_{carb}$	$\pm\sigma$
1332.50	-22.56	0.30	0.44	0.52	21.48	-13.70	0.20	-5.35	0.05
1335.00	-22.12	0.30	0.51	0.52	56.65				
1337.55	-22.72	0.30	1.03	0.52	74.88	-16.33	0.20	-6.79	0.05
1339.41	-22.67	0.30	0.65	0.52	3.56				
1342.68	-23.87	0.30	0.45	0.52	30.49	-16.26	0.20	-8.51	0.05
1345.35	-23.58	0.30	0.89	0.52	1.58				
1349.18	-24.80	0.30	0.41	0.52	30.07	-15.49	0.20	-7.93	0.05
1352.75	-24.46	0.30	0.58	0.52	19.91				
1355.00	-19.34	0.30	0.67	0.52	58.71	-16.41	0.20	-8.61	0.05
1357.19	-24.70	0.30	0.55	0.52	5.94				
1359.58	-24.84	0.30	0.60	0.52	7.42	-13.91	0.20	-6.85	0.05
1363.45	-24.78	0.30	0.63	0.52	4.10				
1365.23	-25.34	0.30	0.59	0.52	14.27	-17.12	0.20	-9.14	0.05
1367.20	-26.37	0.30	1.37	0.52	2.57				
1370.38	-23.21	0.30	0.51	0.52	2.09				
1373.45	-24.15	0.30	0.50	0.52	4.95				
1374.56	-25.13	0.30	0.76	0.52	11.42	-16.20	0.20	-9.07	0.05
1377.78	-25.14	0.30	0.57	0.52	2.78				
1379.56	-25.90	0.30	0.68	0.52	6.41	-15.42	0.20	-7.71	0.05
1384.82	-24.05	0.30	0.98	0.52	1.14				

4.3 Sulfur Data

The full sulfur isotopic data are listed in Table 4.2. Analyses are presented for bulk rock as well as for separate pyrite segregations. Microphotographs of pyrite as segregations and spots of analysis are illustrated in Fig. 4.7. Because the Batatal Formation core has three intervals with different isotopic characteristics (see Fig. 4.3), each of these intervals will be described below.

4.3.1 $\delta^{34}S$ and $\Delta^{33}S$ data

The Lower Black Shale Interval

The lower black shale interval (between 1385 and 1320 meters of the core) in the Batatal Formation represents uniform facies. Sulfur content in most of the samples is less than 0.1%. Pyrite is present in the form of fine disseminated grains in the sample matrix and rare pyrite concretions up to three cm size, as well as deformed layers of pyrite up to four cm thickness (see Fig. 2.4). Nineteen multiple sulfur isotopic analyses of sulfur extracted from bulk rocks and three analysis of sulfur extracted from pyrite nodules were undertaking using SF_6 technique and measurement with a Thermo FinniganMat 253 in the University of Maryland, Geology Department. Thirty-two analyses of bulk rock and six analyses of pyrites were undertaken using SO_2 technique with an Isoprime-IRMS.

The $\delta^{34}S$ values vary from -9.73 to +0.09‰ in bulk rock. Pyrites have $\delta^{34}S$ close to the same bulk rock with differences of about 2‰ (see Fig. 4.7 for sample 1359.84). Most negative $\delta^{34}S$ values are recognized in the middle of the lower interval

($\sim$ 1360-1350 m depth) with ^{32}S depleting upwards up to almost 0‰ near shale-interval boundary. The $\Delta^{33}S$ values from the lower interval are positive (ranging from +0.48 to +0.12‰, except in the sample GDR-1321.50 with a value of -0.21‰) and notably uniform for this stratigraphic unit with an average value +0.30‰.

The Carbonate Interval

Sulfur content in carbonates (between 1320 and 1250 meters of the GDR-core) is less than 0.1% but pyrite does form thin layers and enriched beds with 1-2 mm pyrite grains. The first measurements were conducted for recognizable drilled pyrite grains or laminae. After identifying highly negative $\Delta^{33}S$ values, carbonate samples were powdered and acidified for using CRS extraction and conducted using highly precise sulfur isotopic measurements with the Thermo FinniganMat 253.

Carbonates have the most negative $\delta^{34}S$ values among all samples in the Batatal Formation with an average value of about -10‰ for bulk analysis. The most negative $\delta^{34}S$, as low as -29.5‰, was derived from drilled 1-2mm pyrite grains in sample GDR-1266.72. This maybe the most negative $\delta^{34}S$ value yet measured from the Neoarchean rocks. The bulk rock measurement from the same sample has a $\delta^{34}S$ value -8.82‰. The sulfur isotopic composition and pyrite morphology do not demonstrate any correlations, but the remarkable heterogeneity of the samples is striking.

In contrast with the lower shale interval, carbonates have negative $\Delta^{33}S$ reaching one of the most negative values seen for Neoarchean rocks, as low as -2.69‰ (sample GDR-1308.80). Average $\Delta^{33}S$ value for all carbonate samples is -1.8$\pm$0.5‰. The $\Delta^{33}S$ values of bulk rock and pyrite segregation analysis have similar composi-

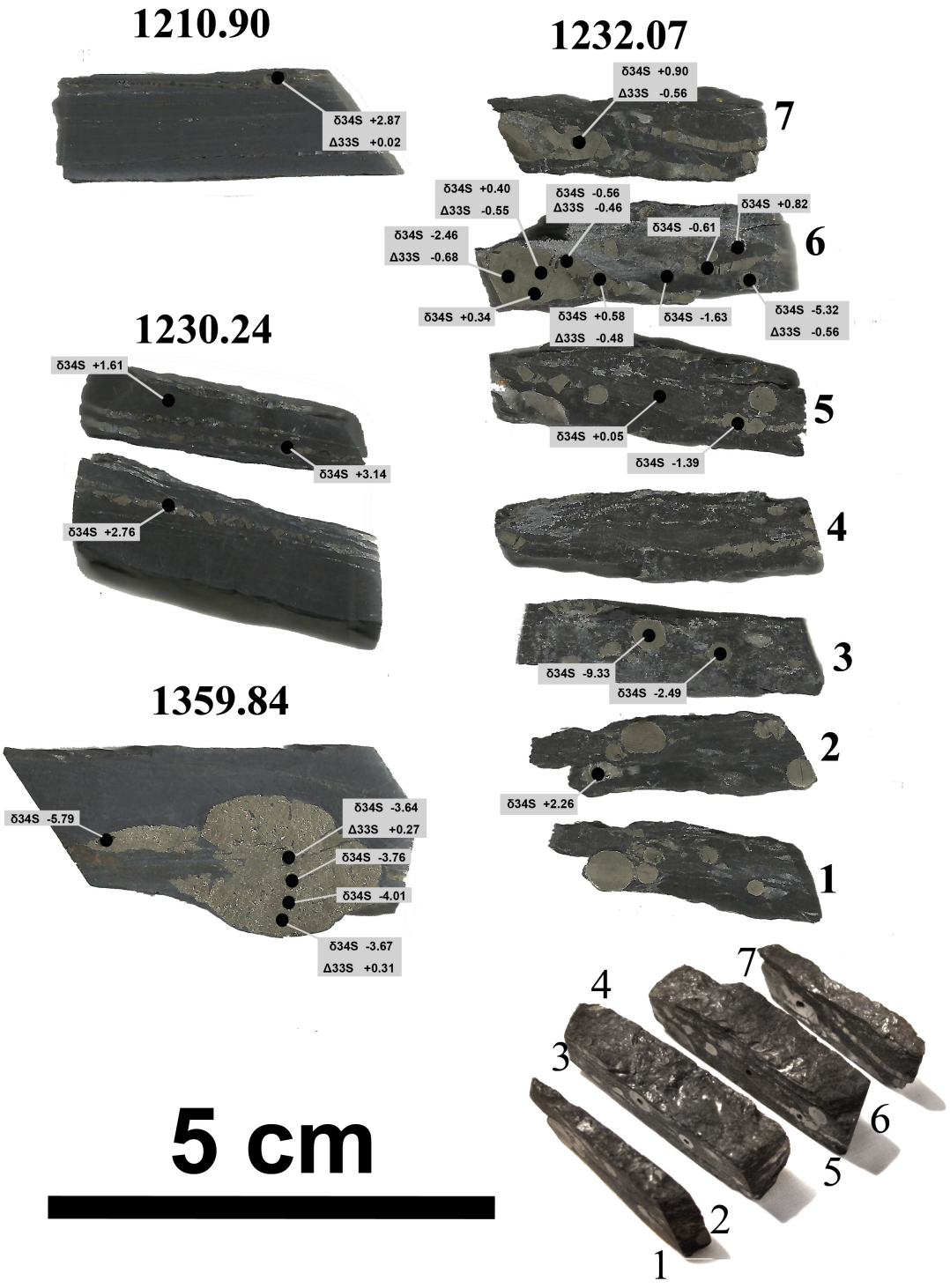

Figure 4.7: Photographs of drill-core samples with sulfur data for each spot

tion but usually $\Delta^{33}S$ values in pyrites are more negative, and the greatest contrast is seen in the sample GDR-1266.72 where bulk rock is characterized by $\Delta^{33}S$ equal to -0.41‰ and pyrite grains have -1.76‰. As seen in Fig. 4.3 $\Delta^{33}S$ values from the bottom ($\sim$ 1320m depth) of the carbonate interval upwards decrease until 1308 m depth acquiring a $\Delta^{33}S$ value -2.69‰. Above this depth, $\Delta^{33}S$ values increase, fluctuating between ca. -2 and -1.5‰ for the next 50 meters of the core.

The Upper Black Shale Interval

The upper shale interval (between 1250 and 1210 meters in the GDR-117 core) has heterogeneous $\delta^{34}S$ and $\Delta^{33}S$ compositions. Samples from the upper black shale were analyzed intensively (see Fig. 4.2 and 4.7) due to high sulfur content (up to 5.23%) and the presence of several types of pyrite. Samples from the 1230-1241 m interval have a number of pyrite nodules, crystals and layers with different features and isotopic compositions. The $\delta^{34}S$ values in bulk rock samples vary between -13.7 and +2.92‰. From the bottom upwards, $\delta^{34}S$ values decreased to values as low as -13.7‰ until 1243 m depth. Above this depth the black shales are enriched in pyrite, carbonate, and chert. The source of sulfur for pyrite nodules and layers were significant enough to form large segregations (see Fig. 2.4). As samples from above 1243 meters are heterogeneous and have pyrite segregations, the isotopic composition of bulk rock composition might not reflect just one process but likely mixing of several sulfur sources.

Pyrite grains with a size greater than 1.0 mm from the samples were drilled and analyzed to compare with bulk rock sulfur isotopic composition . The samples at 1232.07 and 1230.24 m depth were analyzing in detail (Fig. 4.7). These samples

contain spherical pyrite nodules with negative $\delta^{34}S$ values as low as -9.3‰, pyrite associated with quartz with near zero or positive $\delta^{34}S$ values up to +2.3‰, and pyrite crystals in carbonate-quartz layers with $\delta^{34}S$ values up to +3.1‰. In these samples the matrix is enriched in organic matter, and pyrite has sulfur isotopic compositions close to zero or only slightly positive. Thus, the range in sulfur isotopic compositions of pyrites and macroscopic observations of the concretions and pyritic laminations allow us to conclude that there may have been several sources of sulfur during or after deposition of the upper black shale interval.

The $\Delta^{33}S$ values of bulk rock samples from this interval reveal strong mass-independent fractionation signatures (Fig. 4.3), varying from -2.0 to about +2.5‰. The largest positive $\Delta^{33}S$ (+2.5‰) value was measured in the sample from 1228.45 m depth, immediately after the pyrite-enriched 10 m interval. A negative $\Delta^{33}S$ value on the interval below 1243 m in the upper shale interval is similar to a value recorded in the underlying carbonate. Detailed analysis of pyrite nodules (see Fig. 4.7) from the sample GDR-1232.07 demonstrate a range of $\Delta^{33}S$ between -0.46 and -0.70‰ while bulk rock $\Delta^{33}S$ value is +0.14‰, probably reflecting the composition of disseminated pyrite. From the 1220 meter depth of the GDR-117 core upwards, $\Delta^{33}S$ values are close to zero (Fig. 4.8). One of the interpretations is a mixing of mass-independent signals, that is related to nearly complete oxidation of positive-$\Delta^{33}S$-bearing atmospheric S_8.

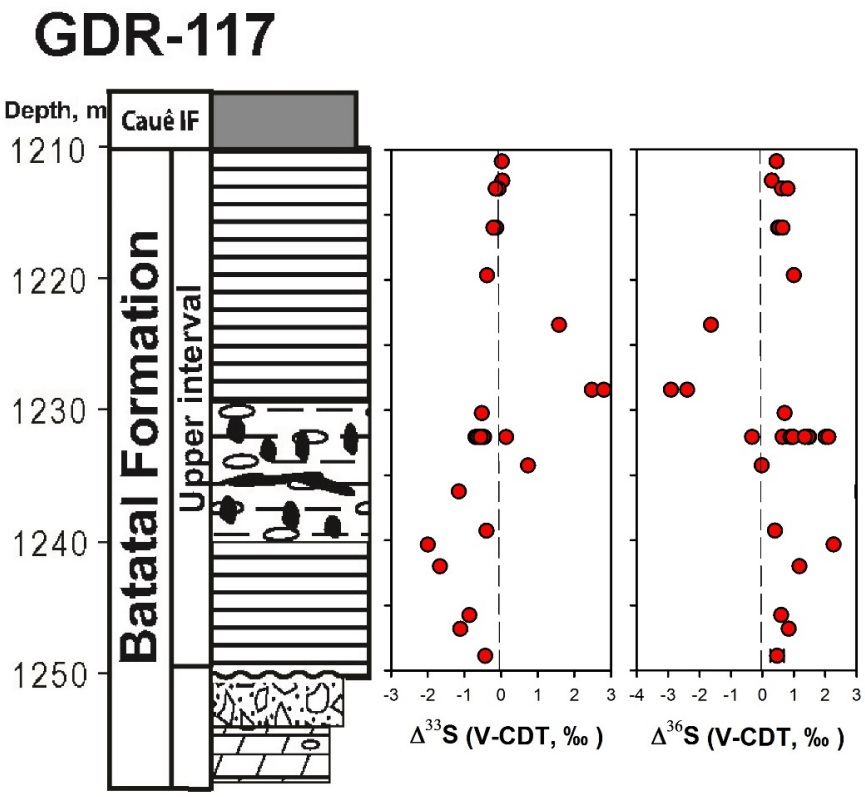

Figure 4.8: Plot of $\Delta^{33}S$ and $\Delta^{36}S$ values against depth in the upper interval of the GDR-117 core. As seen, above 1220 meter depth $\Delta^{33}S$ values become close to zero value.

Table 4.2: Sulfur isotopic composition of samples from the GDR-117 core. MS is a type of mass-spectrometer: EA - Eurovector Elemental Analizer coupled to an Isoprime-IRMS (measurements of SO_2); FM 253 - ThermoFinnigan MAT 253 (measurements of SF_6).

Samples	**Depth, m**	**MS**	**Type**	$\delta^{34}S$	$\pm\sigma$	$\Delta^{33}S$	$\pm\sigma$	$\Delta^{36}S$	$\pm\sigma$
GDR-1210.90P	1210.90	FM253	pyrite	2.87	0.14	0.02	0.008	0.45	0.20
GDR-1210.90	1210.90	EA	bulk	2.92	0.30				
GDR-1210.90	1210.90	EA	pyrite	2.93	0.30				
GDR-1212.38	1212.38	FM 253	bulk	-1.80	0.14	0.04	0.008	0.30	0.20
GDR-1212.38	1212.38	EA	pyrite	2.47	0.30				
GDR-1213.00P	1213.00	FM 253	bulk	-1.89	0.14	-0.06	0.008	0.62	0.20
GDR-1213.00P	1213.00	FM253	pyrite	-1.68	0.14	-0.15	0.008	0.80	0.20
GDR-1213.00	1213.00	EA	bulk	-6.83	0.30				
GDR-1213.00	1213.00	EA	pyrite	-1.51	0.30				
GDR-1214.07	1214.07	EA	bulk	-6.30	0.30				
GDR-1214.07	1214.07	EA	pyrite	-1.63	0.30				
GDR-1215.20	1215.20	EA	bulk	-2.47	0.30				
GDR-1216.00	1216.00	FM 253	bulk	-0.70	0.14	-0.16	0.008	0.50	0.20
GDR-1216.00	1216.00	FM 253	bulk	-1.04	0.14	-0.13	0.008	0.53	0.20
GDR-1216.00P	1216.00	FM253	pyrite	-2.29	0.14	-0.21	0.008	0.64	0.20
GDR-1216.00	1216.00	EA	bulk	-1.11	0.30				
GDR-1216.00	1216.00	EA	pyrite	-2.14	0.30				
GDR-1217.66	1217.66	EA	bulk	-3.03	0.30				
GDR-1219.65	1219.65	FM 253	bulk	-1.17	0.14	-0.38	0.008	1.00	0.20
GDR-1219.65	1219.65	EA	bulk	-1.74	0.30				
GDR-1219.65	1219.65	EA	pyrite	-0.92	0.30				
GDR-1222.65	1222.65	EA	bulk	-2.61	0.30				
GDR-1223.46	1223.46	FM 253	bulk	-1.64	0.14	1.58	0.008	-1.63	0.20

Continued on next page

Table 4.2 – continued from previous page

Samples	Depth, m	MS	Type	$\delta^{34}S$	$\pm\sigma$	$\Delta^{33}S$	$\pm\sigma$	$\Delta^{36}S$	$\pm\sigma$
GDR-1223.46	1223.46	EA	bulk	-1.44	0.30				
GDR-1226.53	1226.53	EA	bulk	-3.89	0.30				
GDR-1228.35	1228.35	EA	bulk	-3.40	0.30				
GDR-1228.45	1228.45	FM 253	bulk	-2.30	0.14	2.48	0.008	-2.39	0.20
GDR-1228.45	1228.45	FM 253	bulk	-3.38	0.14	2.80	0.008	-2.91	0.20
GDR-1228.45	1228.45	EA	bulk	-3.24	0.30				
GDR-1230.24	1230.24	FM 253	bulk	2.82	0.14	-0.52	0.008	0.71	0.20
GDR-1230.24	1230.24	EA	bulk	2.12	0.30				
GDR-1230.24	1230.24	EA	pyrite	3.14	0.30				
GDR-1230.24	1230.24	EA	pyrite	1.61	0.30				
GDR-1230.24	1230.24	EA	pyrite	2.76	0.30				
GDR-1232.07	1232.00	EA	pyrite	-2.49	0.30				
GDR-1232.07	1232.00	EA	pyrite	-3.29	0.30				
GDR-1232.07	1232.07	FM 253	bulk	0.29	0.14	0.14	0.008	-0.33	0.20
GDR-1232.07P-5	1232.07	FM253	pyrite	-5.32	0.14	-0.56	0.008	2.01	0.20
GDR-1232.07P-2	1232.07	FM253	pyrite	0.40	0.14	-0.55	0.008	2.10	0.20
GDR-1232.07P-8	1232.07	FM253	pyrite	-8.59	0.14	-0.70	0.008	1.49	0.20
GDR-1232.07P-3	1232.07	FM253	pyrite	-0.56	0.14	-0.46	0.008	0.64	0.20
GDR-1232.07P-4	1232.07	FM253	pyrite	0.58	0.14	-0.48	0.008	0.89	0.20
GDR-1232.07P-10	1232.07	FM253	pyrite	-2.46	0.14	-0.68	0.008	1.46	0.20
GDR-1232.07P-10	1232.07	FM253	pyrite	-2.12	0.14	-0.63	0.008	0.97	0.20
GDR-1232.07P-15	1232.07	FM253	pyrite	0.90	0.14	-0.56	0.008	1.35	0.20
GDR-1232.07	1232.07	EA	bulk	0.15	0.30				
GDR-1232.07	1232.07	EA	pyrite	2.45	0.30				
GDR-1232.07-1	1232.07	EA	pyrite	0.34	0.30				
GDR-1232.07-2	1232.07	EA	pyrite	0.80	0.30				

Continued on next page

Table 4.2 – continued from previous page

Samples	Depth, m	MS	Type	$\delta^{34}S$	$\pm\sigma$	$\Delta^{33}S$	$\pm\sigma$	$\Delta^{36}S$	$\pm\sigma$
GDR-1232.07-3	1232.07	EA	pyrite	-0.49	0.30				
GDR-1232.07-4	1232.07	EA	pyrite	-1.09	0.30				
GDR-1232.07-5	1232.07	EA	pyrite	-4.47	0.30				
GDR-1232.07-6	1232.07	EA	pyrite	-0.61	0.30				
GDR-1232.07-7	1232.07	EA	pyrite	0.82	0.30				
GDR-1232.07-8	1232.07	EA	pyrite	-9.33	0.30				
GDR-1232.07-12	1232.07	EA	pyrite	-1.39	0.30				
GDR-1232.07-14	1232.07	EA	pyrite	2.26	0.30				
GDR-1232.07-15	1232.07	EA	pyrite	1.49	0.30				
GDR-1232.07-13	1232.07	EA	pyrite	0.05	0.30				
GDR-1232.07-11	1232.07	EA	pyrite	-1.63	0.30				
GDR-1234.25	1234.25	FM 253	bulk	2.73	0.14	0.74	0.008	-0.02	0.20
GDR-1234.25	1234.25	EA	bulk	2.26	0.30				
GDR-1236.25	1236.25	FM 253	bulk	2.50	0.14	-1.15	0.008	3.01	0.20
GDR-1236.25	1236.25	EA	bulk	2.82	0.30				
GDR-1238.25	1238.25	EA	pyrite	0.08	0.30				
GDR-1239.27	1239.27	FM 253	bulk	2.50	0.14	-0.40	0.008	0.40	0.20
GDR-1239.27	1239.27	EA	bulk	1.67	0.30				
GDR-1239.27	1239.27	EA	pyrite	0.60	0.30				
GDR-1239.27	1239.27	EA	pyrite	-0.40	0.30				
GDR-1240.33P	1240.33	FM253	pyrite	0.32	0.14	-2.00	0.008	2.27	0.20
GDR-1240.33	1240.33	EA	pyrite	0.34	0.30				
GDR-1242.00P	1242.00	FM253	pyrite	-2.11	0.14	-1.66	0.008	1.18	0.20
GDR-1242.68	1242.00	EA	bulk	-3.36	0.30				
GDR-1242.00	1242.00	EA	pyrite	-2.99	0.30				
GDR-1243.26	1243.26	EA	bulk	-13.47	0.30				

Continued on next page

Table 4.2 – continued from previous page

Samples	**Depth, m**	**MS**	**Type**	$\delta^{34}S$	$\pm\sigma$	$\Delta^{33}S$	$\pm\sigma$	$\Delta^{36}S$	$\pm\sigma$
GDR-1243.26	1243.26	EA	bulk	-13.69	0.30				
GDR-1245.35	1245.00	EA	bulk	-7.29	0.30				
GDR-1245.75P	1245.75	FM253	pyrite	-3.25	0.14	-0.86	0.008	0.60	0.20
GDR-1245.75	1245.75	EA	pyrite	-3.23	0.30				
GDR-1246.81	1246.81	FM 253	bulk	-7.56	0.14	-1.11	0.008	0.84	0.20
GDR-1246.81	1246.81	EA	bulk	-8.94	0.30				
GDR-1246.81	1246.81	EA	bulk	-7.97	0.30				
GDR-1247.70	1247.70	EA	bulk	-1.61	0.30				
GDR-1248.88	1248.88	EA	bulk	-4.45	0.30				
GDR-1248.88	1248.88	FM 253	bulk	-4.22	0.14	-0.43	0.008	0.47	0.22
GDR-1251.90	1251.90	FM 253	bulk	-5.99	0.14	-1.44	0.008	1.46	0.20
GDR-1256.33	1256.33	FM 253	bulk	-10.33	0.14	-1.72	0.008	1.69	0.20
GDR-1256.33	1256.33	EA	pyrite	-16.79	0.30				
GDR-1261.90	1261.90	FM 253	bulk	-4.79	0.14	-0.87	0.008	1.19	0.20
GDR-1261.90P	1261.90	FM253	pyrite	-13.69	0.14	-1.36	0.008	1.38	0.20
GDR-1261.90	1261.90	EA	pyrite	-14.05	0.30				
GDR-1266.72	1266.72	FM 253	bulk	-8.82	0.14	-0.41	0.008	0.53	0.20
GDR-1266.72P	1266.72	FM253	pyrite	-29.46	0.14	-1.76	0.008	1.91	0.20
GDR-1266.72	1266.72	EA	pyrite	-29.59	0.30				
GDR-1266.72	1266.72	EA	pyrite	-29.95	0.30				
GDR-1272.70	1272.70	FM 253	bulk	-7.32	0.14	-1.41	0.008	1.87	0.20
GDR-1272.70P	1272.70	FM253	pyrite	-3.07	0.14	-1.85	0.008	2.71	0.20
GDR-1272.70	1272.70	EA	pyrite	-3.59	0.30				
GDR-1272.70	1272.70	EA	pyrite	-3.32	0.30				
GDR-1278.10	1278.10	FM 253	bulk	-12.07	0.14	-1.68	0.008	1.46	0.20
GDR-1282.47	1282.47	FM 253	bulk	-12.31	0.14	-1.89	0.008	1.94	0.20

Continued on next page

Table 4.2 – continued from previous page

Samples	Depth, m	MS	Type	$\delta^{34}S$	$\pm\sigma$	$\Delta^{33}S$	$\pm\sigma$	$\Delta^{36}S$	$\pm\sigma$
GDR-1286.60	1286.60	FM 253	bulk	-10.67	0.14	-1.90	0.008	1.85	0.20
GDR-1291.65	1291.65	FM 253	bulk	-13.85	0.14	-1.93	0.008	2.70	0.20
GDR-1291.65	1291.65	EA	pyrite	-14.11	0.30				
GDR-1296.64	1296.64	FM 253	bulk	-13.32	0.14	-1.90	0.008	1.95	0.20
GDR-1298.65	1298.65	FM 253	bulk	-9.33	0.14	-1.66	0.008	1.46	0.20
GDR-1298.65P	1298.65	FM253	pyrite	-11.67	0.14	-2.01	0.008	1.91	0.20
GDR-1298.65	1298.65	EA	pyrite	-12.38	0.30				
GDR-1302.23	1302.23	FM 253	bulk	-7.13	0.14	-1.95	0.008	2.19	0.20
GDR-1305.00	1305.00	FM 253	bulk	-13.10	0.14	-2.35	0.008	1.94	0.20
GDR-1305.00	1305.00	EA	pyrite	-10.42	0.30				
GDR-1308.00P	1308.00	FM253	pyrite	-12.45	0.14	-2.54	0.008	2.53	0.20
GDR-1308.00	1308.00	EA	pyrite	-12.93	0.30				
GDR-1308.00	1308.00	FM 253	bulk	-14.04	0.14	-2.69	0.008	2.31	0.20
GDR-1309.91	1309.91	FM 253	bulk	-10.17	0.14	-2.15	0.008	2.09	0.20
GDR-1311.17	1311.17	FM 253	bulk	-9.52	0.14	-1.82	0.008	1.92	0.20
GDR-1311.17	1311.17	EA	pyrite	-11.54	0.30				
GDR-1313.13	1313.13	FM 253	bulk	-6.96	0.14	-1.11	0.008	1.03	0.20
GDR-1313.13	1313.13	EA	pyrite	-15.45	0.30				
GDR-1316.30	1316.30	FM 253	bulk	-9.03	0.14	-1.75	0.008	1.68	0.20
GDR-1316.30P	1316.30	FM253	pyrite	-14.36	0.14	-2.12	0.008	2.04	0.20
GDR-1316.30	1316.30	EA	pyrite	-14.75	0.30				
GDR-1318.37	1318.37	FM 253	bulk	-6.25	0.14	-1.77	0.008	2.08	0.20
GDR-1320.17	1320.17	FM 253	bulk	0.09	0.14	0.35	0.008	-0.71	0.20
GDR-1320.17	1320.17	EA	bulk	-1.09	0.30				
GDR-1321.50	1321.50	FM 253	bulk	-4.08	0.14	-0.21	0.008	0.34	0.20
GDR-1321.50	1321.50	EA	bulk	-3.65	0.30				

Continued on next page

Table 4.2 – continued from previous page

Samples	Depth, m	MS	Type	$\delta^{34}S$	$\pm\sigma$	$\Delta^{33}S$	$\pm\sigma$	$\Delta^{36}S$	$\pm\sigma$
GDR-1323.55	1323.55	FM 253	bulk	-2.34	0.14	0.21	0.008	-0.01	0.20
GDR-1323.55	1323.55	EA	bulk	-2.22	0.30				
GDR-1325.20	1325.20	FM 253	bulk	-0.35	0.14	0.33	0.008	0.12	0.20
GDR-1325.20	1325.20	EA	bulk	-0.70	0.30				
GDR-1326.00	1326.00	EA	bulk	-1.44	0.30				
GDR-1329.90	1329.90	EA	bulk	-6.52	0.30				
GDR-1332.50	1332.50	EA	bulk	-5.30	0.30				
GDR-1335.00	1335.00	EA	bulk	-12.11	0.30				
GDR-1339.41	1339.41	EA	bulk	-6.23	0.30				
GDR-1340.30	1340.30	EA	bulk	-7.06	0.30				
GDR-1345.35	1345.35	EA	bulk	-7.88	0.30				
GDR-1350.80	1350.80	FM 253	bulk	-6.68	0.14	0.13	0.008	-0.56	0.87
GDR-1350.80	1350.80	EA	bulk	-7.36	0.30				
GDR-1351.69	1351.69	EA	bulk	-7.72	0.30				
GDR-1353.60	1353.60	EA	bulk	-4.46	0.30				
GDR-1355.00	1355.00	FM 253	bulk	-3.62	0.14	0.18	0.008	-0.08	0.20
GDR-1355.00	1355.00	EA	bulk	-7.19	0.30				
GDR-1357.19	1357.19	EA	bulk	-6.80	0.30				
GDR-1359.84	1359.84	FM 253	bulk	-5.89	0.14	0.25	0.008	-0.61	0.20
GDR-1359.84P-4	1359.84	FM253	pyrite	-3.67	0.14	0.31	0.008	-0.85	0.20
GDR-1359.84P-1	1359.84	FM253	pyrite	-3.64	0.14	0.27	0.008	-0.74	0.20
GDR-1359.84	1359.84	EA	bulk	-5.84	0.30				
GDR-1359.84	1359.84	EA	bulk	-3.71	0.30				
GDR-1359.84-1	1359.84	EA	pyrite	-4.54	0.30				
GDR-1359.84-2	1359.84	EA	pyrite	-3.76	0.30				
GDR-1359.84-3	1359.84	EA	pyrite	-4.01	0.30				

Continued on next page

Table 4.2 – continued from previous page

Samples	**Depth, m**	**MS**	**Type**	$\delta^{34}S$	$\pm\sigma$	$\Delta^{33}S$	$\pm\sigma$	$\Delta^{36}S$	$\pm\sigma$
GDR-1359.84-4	1359.84	EA	pyrite	-4.38	0.30				
GDR-1359.84-5	1359.84	EA	pyrite	-5.79	0.30				
GDR-1360.31	1360.31	EA	bulk	-9.73	0.30				
GDR-1362.20	1362.20	EA	bulk	-7.22	0.30				
GDR-1363.45	1363.45	EA	bulk	-6.32	0.30				
GDR-1365.23P	1365.23	FM253	pyrite	-4.30	0.14	0.39	0.008	-0.48	0.20
GDR-1365.23	1365.23	EA	bulk	-5.75	0.30				
GDR-1365.23	1365.23	EA	pyrite	-4.22	0.30				
GDR-1367.20	1367.20	EA	bulk	-6.74	0.30				
GDR-1367.53	1367.53	FM 253	bulk	-3.28	0.14	0.47	0.008	-0.60	0.20
GDR-1367.53	1367.53	EA	bulk	-3.73	0.30				
GDR-1370.38	1370.38	FM 253	bulk	-4.93	0.14	0.43	0.008	-1.45	0.33
GDR-1370.38	1370.38	EA	bulk	-5.35	0.30				
GDR-1373.45	1373.45	FM 253	bulk	-3.58	0.14	0.48	0.008	-0.14	0.20
GDR-1373.45	1373.45	EA	bulk	-4.60	0.30				
GDR-1373.45	1373.45	EA	bulk	-4.12	0.30				
GDR-1374.56	1374.56	EA	bulk	-4.35	0.30				
GDR-1377.51	1377.51	EA	bulk	-4.61	0.30				
GDR-1379.56	1379.56	FM 253	bulk	-2.66	0.14	0.43	0.008	-0.92	0.20
GDR-1379.56	1379.56	EA	bulk	-3.73	0.30				
GDR-1383.19	1383.19	FM 253	bulk	-3.51	0.14	0.12	0.008	-0.19	0.20
GDR-1384.82	1384.82	EA	bulk	-2.49	0.30				
GDR-1385.10	1385.10	EA	bulk	-3.04	0.30				

Chapter 5

Discussion

As discussed above, lithological variations in the Batatal Formation indicate changes in deposition environments associated with relative sea level. The deposition of the Batatal Formation can be divided into two depositional cycles, each starting with black shales and continuing to either carbonate-rich rock or banded-iron formation. One represents a shallowing upward cycle and the other a deeping upward cycle.

The lower interval of the Batatal Formation initiates the first cycle. Here, because at the base of the lower interval black shales are interbedded with clastic sediments, very shallow environments are proposed. Further transgression and deepening caused suppression of terrigenous clastic flux and precipitation of fine-grained black shale. Preservation of organic matter was likely due to high primary microbial productivity and high rate of preservation under anoxic conditions. X-ray diffraction (XRD) data on powdered samples from the lower Batatal shale reveal the presence of siderite, supporting the likelihood of anoxic, but not euxinic, conditions. The increasing carbonate concentration upwards in the GDR-117 core was caused by the consumption of CO_2 by organisms to increase CO_3^{2-} concentration. Because carbon isotopic compositions of organic matter and carbonate in black shale demonstrate coupled enrichment in ^{13}C upwards in the core, the depositional system was likely

closed in terms of carbon availability. A closed sedimentary pore water system is also partially supported by $\delta^{34}S$ values that show small magnitudes of fractionation. However, sulfur isotopic composition in this case is potentially a function of sulfate concentration. The increase in sulfur isotopic fractionation in the middle of the lower interval suggests that SO_4^{2-} concentration may have risen above 200 μM (Habicht et al., 2002).

The transition from the lower shale interval to the carbonate interval is a lithologically gradational transition but is marked by a much sharper isotopic transition. Sulfur, carbon, and oxygen isotopic compositions distinguish the carbonate interval from both underlying and overlying intervals. This sharp isotopic transition is therefore thought to reflect a marked geochemical change. Deposition of carbonates occurred in a photic zone. Here, microbial productivity was high due to availability of sunlight and nutrients, but the rate of organic matter preservation was low, perhaps due to rapid recycling. Sulfur, carbon, and oxygen isotopic compositions of carbonates preserved stable and homogeneous values throughout this part of the core. Microbial sulfate reducers generated significant ^{34}S depletion in pyrite indicating they acted under open-system conditions and probably with sulfate concentration above a threshold value of >200 μM, which is enough to produce large sulfur isotopic fractionation (Habicht et al., 2002).

Breccia at the top of the carbonate interval indicates that the section was most likely exposed and karstified before deposition of the upper shale interval. It is conceivable that brecciation was further promoted by the dissolution of soluble sulfate minerals that formed in very shallow environments. The upper interval starts the

second deepening upwards sedimentary cycle. Because of the high organic carbon contents, it is likely that deposition of the upper black shale occured under reducing conditions with high microbial productivity. Sulfate-reducing bacteria here played an important role as clearly seen in the formation of pyrite-rich layers. Variations in $\delta^{34}S$ and $\Delta^{33}S$ values and high TOC throughout the upper interval indicate high-productivity likely coupled with a high rate of sedimentation. The high sulfur and carbon contents in this interval may also indicate input from a hydrothermal source, or potantially the migration of soluble hydrocarbons. Further transgression pushed facies shoreward and resulted in deposition of the deep water Cauê Iron Formation deposition.

5.1 Evidence for Bacterial Sulfate Reduction

Sulfur isotopic data gives information about the activity of sulfate reducers insofar as their metabolic activities can shift $\delta^{34}S$ of product sulfide. Black shales in the Batatal Formation show a range of $\delta^{34}S$ data from -13.7 to +2.9‰ with an average value around -5‰. If we assume that average isotopic composition of Neoarchean seawater was +10‰ (Farquhar and Wing, 2005; Ono et al., 2003), fractionation in the lower interval ranges between 7 and 24 ‰. This may be attributed seawater sulfate concentration more than 200 μM (Habicht et al., 2002).

The average $\delta^{34}S$ for carbonate samples is about -10‰ with some extremely negative value in pyrite grains as low as -30‰. Perhaps, during the carbonate deposition sulfate reducers played an important role in the formation of the ^{34}S depleted

sulfides in environments where sulfate concentrations exceeded 200 μM. High rates of evaporation of shallow seawater might concentrate sulfate in the carbonate environments and also cause silica enrichment. The lowest $\delta^{34}S$ value is one of the most negative value found in Archean rocks. This might indicate that sulfate concentration might be higher in the shallowest parts of the ocean and lower in deeper parts. The most negative $\delta^{34}S$ values in the equivalent Mt. McRae Shale Formation also come from carbonate facies (Kaufman et al., 2007). It seems possible that the ocean was stratified with respect to sulfate in the Neoarchean.

5.2 Preservation of $\Delta^{33}S$ Signals

Multiple sulfur isotopic data collected over the last decade (see Fig. 1.6) show variable $\Delta^{33}S$ values with prevalence over negative signatures. This dataset, however, is mostly composed of shale analyses, so it is possible that a non-shale complement of carbonate rocks might preserve predominantely negative signature, and thus address the issue of asymmetry in the $\Delta^{33}S$ in the Neoarchean record (see Fig. 1.6). If correct, the carbonate reservoir might close the Archean sulfur cycle.

It was suggested that two separate reservoirs existed in the Archean to preserve distinct $\Delta^{33}S$ signatures (Farquhar et al., 2001; Ono et al., 2003). Photolysis of SO_2 is thought to have produced sulfate with negative $\Delta^{33}S$ values and elemental sulfur with positive $\Delta^{33}S$ values (Farquhar et al., 2000; Ono et al., 2003). Many studies (Farquhar and Wing, 2003; Kaufman et al., 2007; Ono et al., 2003) have suggested that the main source of sulfur in the Archean sulfur cycle was from mixing of

photochemically-derived mass-independent sulfur and mass-dependent sulfur from volcanic sources. Preservation of distinct $\delta^{34}S$ as well as $\Delta^{33}S$ signatures might be controlled by microbial processes, reduction of sulfate and/or elemental sulfur to form pyrite, or oxidation of elemental sulfur to sulfate.

Ono et al. (2003) first suggested the possible importance of lithological control over the distribution and preservation of sulfur signatures on the basis of sulfur isotopic data from Neoarchean Western Australian succession. Ono et al. (2009b) first proposed that distinct sulfur isotopic signatures ($\delta^{34}S$-$\Delta^{33}S$ relations) were preserved according to lithofacies on the basis of data from 2.6 - 2.5 Ga rocks in South Africa. Similarly, the sulfur data from the Batatal Formation suggests that negative $\Delta^{33}S$ signatures are predominantely found in carbonate facies, which would be enriched in atmospheric sulfate, perhaps through evaporative concentration in shallower environments. Atmospheric sulfur with positive $\Delta^{33}S$ values as seen in shales is absent from the Batatal carbonates. This difference is attributed to different pathways for S_8 preservation (in deeper shale environments) or possibly low reactivity of elemental sulfur during carbonate formation. In the Batatal Formation the lower shale and carbonate intervals lithologically have gradational boundary, but geochemically the transition is very sharp (see Fig. 4.3) indicating a change in geochemical processes as progressive regression occurred.

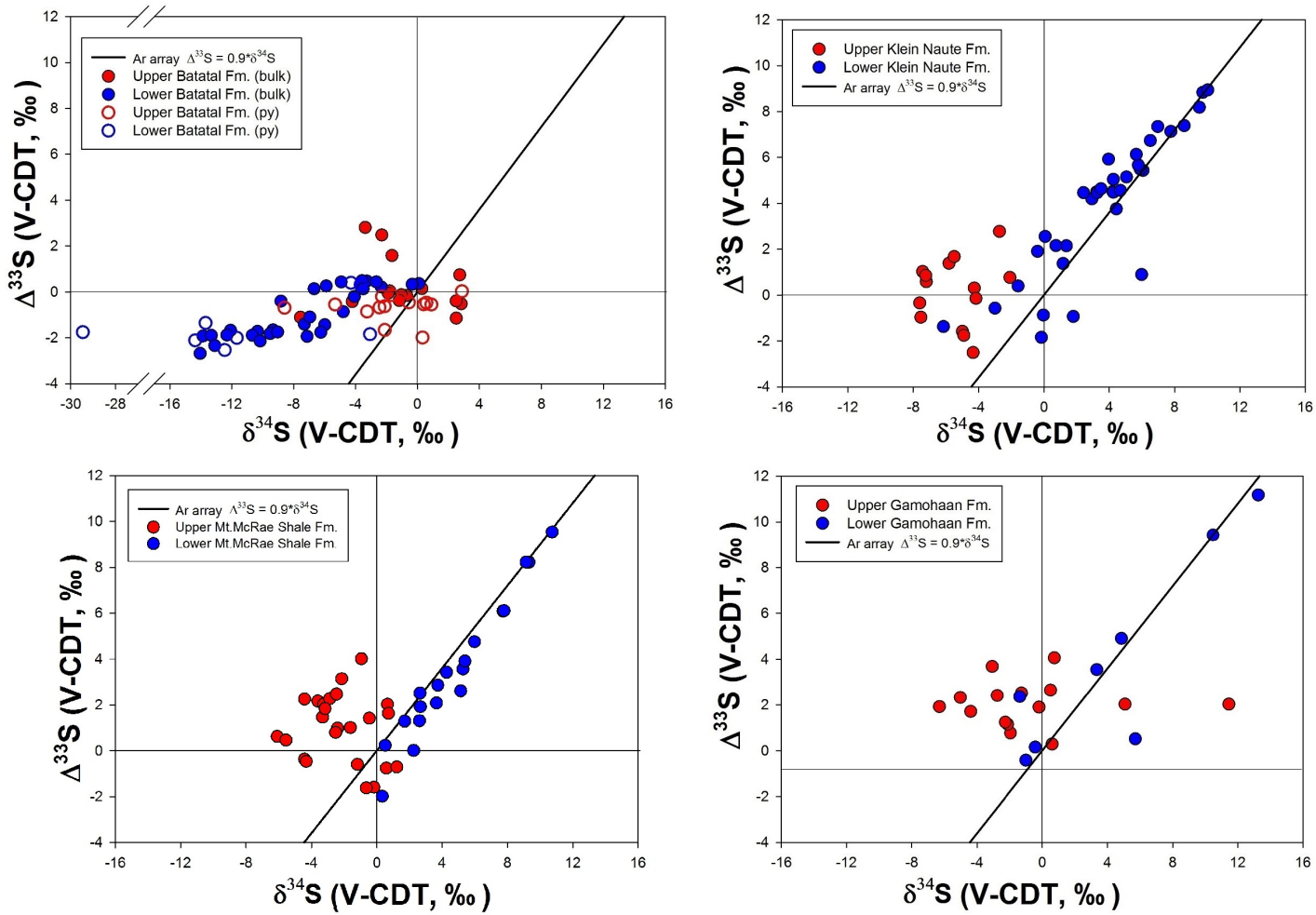

Figure 5.1: Plot of $\delta^{34}S$ vs. $\Delta^{33}S$ of Neoarchean successions is from Kaufman et al. (2007); Kendall et al. (2010). Just bulk rock analysis were used. Solid line is empirically estimated Archean array (Kaufman et al., 2007; Ono et al., 2003). Data from the Batatal Formation is from the current study: the upper Batatal Formation is defined as the upper shale interval, and the lower Batatal Formation comprises the carbonate and lower shale intervals.

Figure 5.1 demonstrates $\delta^{34}S$-$\Delta^{33}S$ relations in equivalent units with ages of $\sim$ 2.5 Ga from South Africa and Western Australia. Each of the successions was divided on the basis of compositional and geochemical differences. The lower part of the Mt. McRae Shale formation is Fe-rich and contains siderite indicating highly reducing conditions (Kaufman et al., 2007). Lower intervals of the Western Australian (the Mt. McRae Shale Formation) and South African (the Klein Naute Formation from the Griqualand Basin and the Gamohaan Formation from the Transvaal Basin) successions indicate consistency in terms of similar $\delta^{34}S$-$\Delta^{33}S$ relations with a slope $\sim$ -0.9 that has been interpreted as the Archean array (Kaufman et al., 2007; Ono et al., 2009b). These Fe-rich intervals preserved the most positive $\Delta^{33}S$ signatures probably due to formation of pyrite through the reaction of monosulfides with atmospherically-derived elemental sulfur. The Batatal Formation in Fig. 5.1 shows completely different $\delta^{34}S$-$\Delta^{33}S$ relationship, with a slope of about -0.2. The most negative $\delta^{34}S$ and $\Delta^{33}S$ values are in carbonates of the Batatal Formation; most analyses from the Western Australian and South African formations are of shales or shaley carbonates. Sulfate-reducing bacteria appear to here played an important role in the Batatal sulfur cycle, producing $\delta^{34}S$ values as low as $\sim$ -30‰, without mixing it with other types of sulfur sources. Thus, sulfate for bacterial metabolism was from atmospherically-derived sulfate with negative $\Delta^{33}S$ signature, and an average sulfate seawater $\Delta^{33}S$ composition of about -2‰ as proposed earlier by Ono et al. (2003).

Similar to the Western Australian and South African successions (Kaufman et al., 2007; Ono et al., 2009b), sideritic intervals in the Batatal Formation are also

associated with positive $\Delta^{33}S$ values. It is possible that the highly reducing conditions necessary for siderite stability promote the reaction of elemental sulfur with iron monosulfide to preferentially form pyrite.

Carbonates have not previously been recognized as a host for strongly negative $\delta^{34}S$ and $\Delta^{33}S$ compositions, but earlier publications (Ono et al., 2003; Partridge et al., 2008) report limited data from Archean carbonates with negative sulfur signatures ($\delta^{34}S$ and $\Delta^{33}S$) (see Fig. 5.2). Carbonates may thus be an overlooked sink for negative $\Delta^{33}S$ and/or $\delta^{34}S$. Recently SIMS analysis of microscopic pyrites from South African ca. 2.5 Ga rocks (Farquhar et al., 2013) demonstrate strongly negative $\delta^{34}S$ with negative $\Delta^{33}S$. However, bulk rock analysis of the host rocks mainly shows small fractionation, and the prevalent $\delta^{34}S$ values are positive with only a few negative compositions (Zerkle et al., 2012). It is possible that preservation of mostly negative $\Delta^{33}S$ in carbonates is related to the inhibition of elemental sulfur reactions in the shallow, and perhaps more oxidized portion of water column.

5.3 Neoarchean $\Delta^{33}S$-$\Delta^{36}S$ Relationships

It was found by Farquhar et al. (2001) that relationships between minor sulfur isotopes in Archean samples define a $\Delta^{36}S/\Delta^{33}S$ array of $\sim$ -0.9 that is similar to experimentally observed relations during SO_2 photolysis using ArF and Xe lamps (Farquhar et al., 2000). Subsequent work by Kaufman et al. (2007) and Farquhar et al. (2007) revealed variations about this slope that were interpreted to reflect changing atmospheric chemistry. The $\Delta^{36}S/\Delta^{33}S$ relations from the Batatal For-

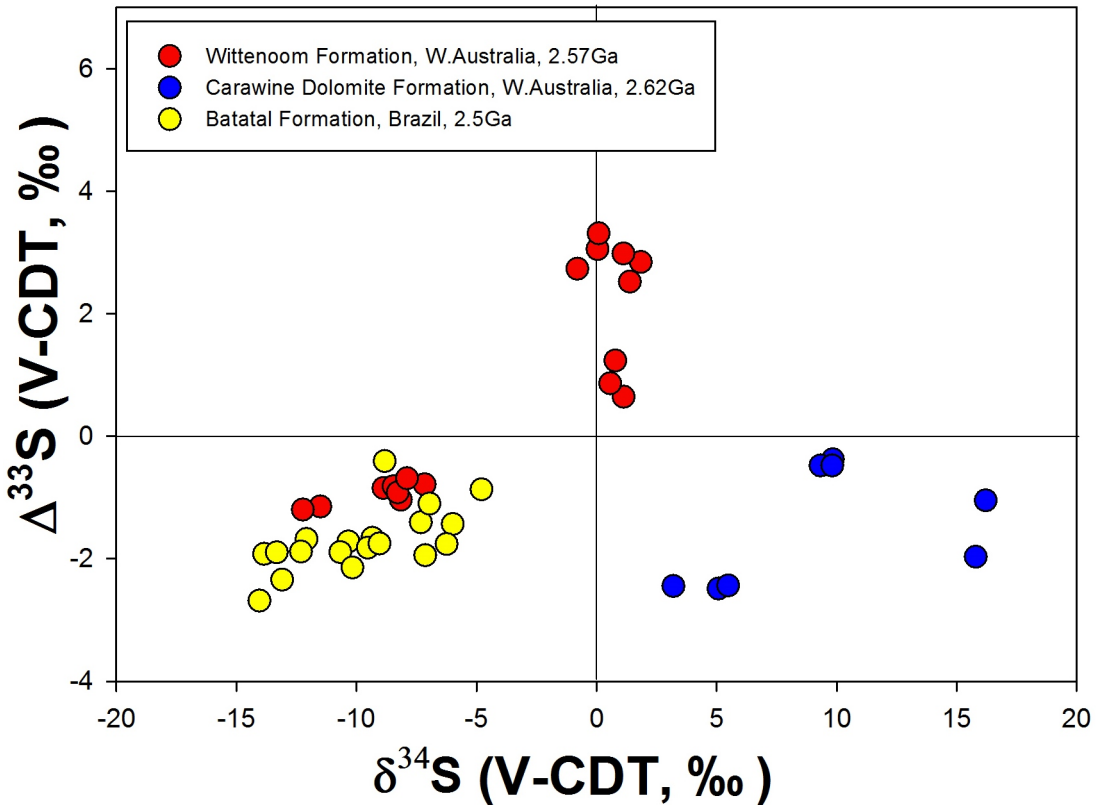

Figure 5.2: Plot of $\delta^{34}S$ vs. $\Delta^{33}S$ values from Neoarchean carbonates. Data are from Ono et al. (2003); Partridge et al. (2008) and this study.

mation follows the previously defined Archean array (see Fig. 5.3) and so is consistent with other Neoarchean successions. This is an additional confirmation about global distribution of MIF-S in Archean derived from the photochemical reactions in almost free-oxygen atmosphere ($< 10^{-5}$ PAL from the model of Pavlov and Kasting (2002)). Records from the Batatal Formation are characterized by the absence of highly positive $\Delta^{33}S$ with the maximum value +2.8‰ whilst African and Australian records exhibit values as high as +11.2‰. Ono et al. (2003) modeled that large $\Delta^{33}S$ signatures can be received from high-altitude S_8 whereas ground level S_8 carries smaller $\Delta^{33}S$ signatures. The latter might be the case for the Batatal Formation where small positive $\Delta^{33}S$ signatures were preserved due to isotope mixing

with other sulfur species.

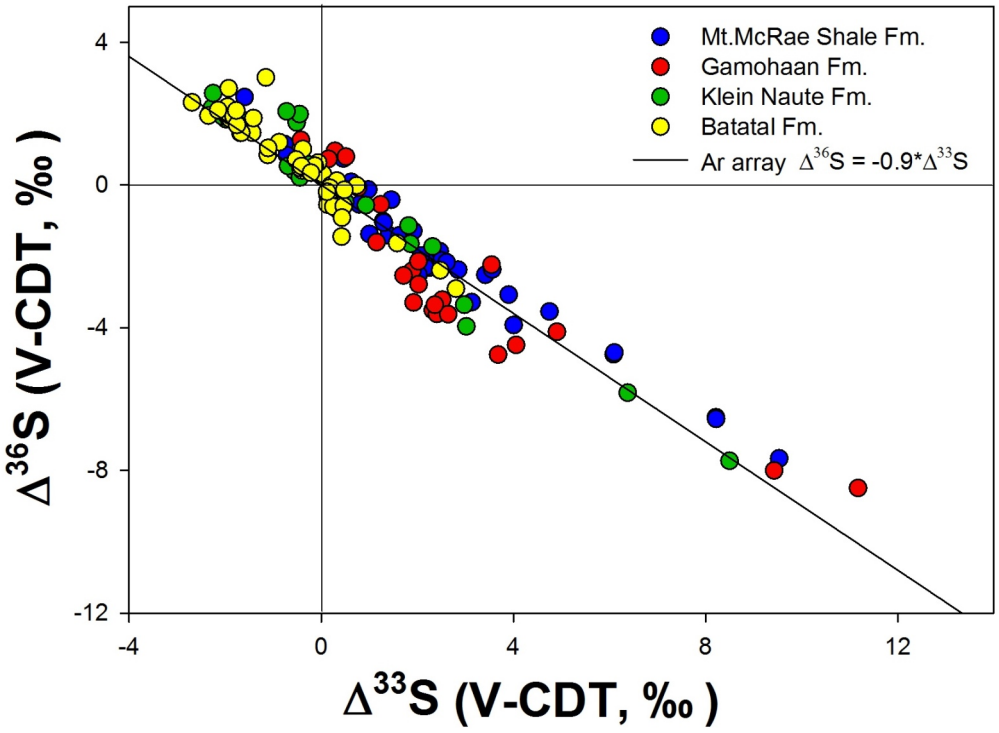

Figure 5.3: Plot of $\Delta^{33}S$ vs. $\Delta^{36}S$ data of Neoarchean successions is from Kaufman et al. (2007); Ono et al. (2009a). Just bulk rock analysis were used. The solid line is the so-called Archean atmospheric array (Farquhar et al., 2001). Data from the Batatal Formation is from the current study.

5.4 Carbon Isotope Data in the Neoarchean Successions

It was discovered during this study of the Batatal Formation that the fractionation of carbon isotopes between organic carbon and carbonate carbon is constant in all lithofacies around 15‰. This fractionation is much smaller than observed in other studies of Neoarchean successions (e.g. the Mt. McRae Shale and Klein Nate formations) (Fischer et al., 2009; Kaufman et al., 2007) where fractionation is almost 30‰ with $\delta^{13}C_{org}$ values with an average $\sim$ -35‰ while in Brazilian records, the average $\delta^{13}C_{org}$ value is -20‰.

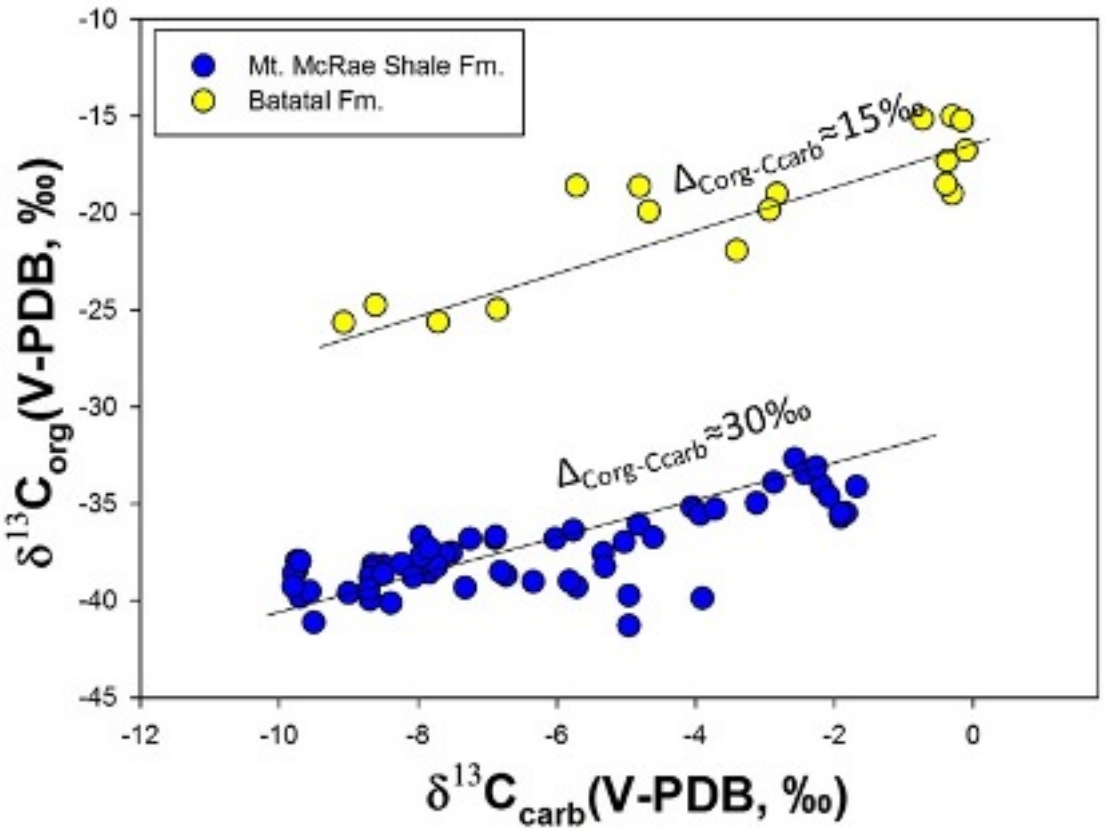

Figure 5.4: Plot of $\delta^{13}C_{org}$ vs. $\delta^{13}C_{carb}$ for the Batatal and Mt.McRae Shale formations from this study and Kaufman et al. (2007), respectively.

As demonstrated in Fig. 5.4 the range of $\delta^{13}C_{carb}$ from the Batatal and Mt. McRae Shale formations is almost identical while $\delta^{13}C_{org}$ differs by 15‰. Such parallel trends between the Batatal and Mt. McRae Shale formations suggest strong differences in environmental conditions at which they were formed. Metamorphism could cause decreasing in $\Delta_{org-carb}$ fractionation (Des Marais, 2001), but petrological of the Batatal core samples supports the view that carbon isotopic signatures are likely to be primary.

Modern distribution of $\delta^{13}C$ in surface particulate organic matter in oceans suggest that at lower latitude and thus at higher temperature, $\delta^{13}C_{org}$ values are much higher than at higher latitude and at lower temperature. This occurs because

of CO_2-limiting conditions (Goericke and Fry, 1994). Assuming that the minimum depositional time of the Batatal Formation around 8 Ma (using an average sedimentation rate 2cm/1000 yrs; from Wignall (1994)), preservation of constant enriched $\delta^{13}C_{org}$ signatures through this time with a hiatus and different lithological environments (carbonate and shale) indicates that the Batatal Formation was formed in environments with CO_2-limitation compared with the environment in which the Mt. McRae Shale Formation was deposited. Such condition might be achieved if the Batatal Formation were deposited at higher temperature and/or lower latitudes. Following that the modern $\delta^{13}C_{org}$ - temperature dependence in surface water particulate organic carbon, minimum differences in temperature between the Batatal and Mt. McRae Shale formation would have been 15° Celsius. Latitudinal speculations are more complicated as 2.5 Ga years ago the Sun had less luminosity (Sagan and Mullen, 1972) and position of Vaalbara supercontinent still is a matter of debate (de Kock et al., 2009).

Chapter 6

6.1 Conclusions

Elemental and isotopic time-series study of the GDR-117 core from Brazil complements knowledge about the Neoarchean sulfur cycle and system atmosphere - ocean system derived from studies of equivalent strata in Western Australia and South Africa. The Batatal Formation preserves distinct mass-independent fractionation of sulfur isotopes signatures resulted from the atmospheric chemical reactions and follows the array $\Delta^{36}S/\Delta^{33}S \sim$ -1. On the basis of the $\delta^{34}S$ measurements strong evidence for active sulfate-reduction in the Neoarchean has been discovered. A comparison of data from the Batatal Formation and coincident succesions on other continents (the Mt. McRae Shale Formation, Western Australia, and Klein Naute and Gamohaan formations, South Africa) indicates better preservation of sulfate-reduction processes in the Batatal Formation. This may be due to conditions that prevented mixing with atmospheric elemental sulfur carried positive $\Delta^{33}S$ possibly deposition in shallower environment where carbonates formed relatively rapidly. Analysis of carbonates from the Batatal Formation demonstrate some of the most negative $\Delta^{33}S$ signal in bulk rock derived from the oceanic sulfate reservoir. These data exhibit different pathways of distinctive MIF signal preservation: sulfate with negative $\Delta^{33}S$ tends to be preserved in shallower lithofacies with low organic matter. Positive $\Delta^{33}S$ preserved at deeper lithofacies and diluted with negative $\Delta^{33}S$

signal and sulfate-reduction signature, that is not observed in bulk rock analysis of the African and Australian successions, but can be found by precise spot analysis of sedimentary pyrite. $\delta^{34}S$-$\Delta^{33}S$ relation demonstrates that the Batatal data do not follow early proposed $\Delta^{33}S/\Delta^{34}S$ Archean array ($\sim$ - 0.9) but follow an array $\sim$ -0.2, providing strong evidence for sulfate reduction. Sulfate concentration of seawater during the Batatal Fm. deposition, on the basis of sulfur isotope fractionation, was higher than early proposed 200 μM threshold for the Archean.

Carbon isotope analysis demonstrated that the sedimentary rocks from the Batatal Formation are enriched in ^{13}C, have higher $\delta^{13}C_{org}$, and differ from Neoarchean data with a fractionation of 15‰. These results indicate that the Batatal Formation was formed at carbon-limited conditions possibly in a hotter shallower area, probably at lower latitude than the Neoarchean Australian and African successions.

6.2 Future work

To better understand the environmental conditions under which each of the Batatal interval was formed, proxies such as iron-speciation study and redox sensitive elements study might be applied. The current study illustrates how carbonate rocks in the Archean may be a host for negative $\Delta^{33}S$ and $\delta^{34}S$ signatures. Further work should be focused on studying other Archean carbonates and defining the chemical context of the distinct MIF signatures. This will provide a better understanding of the sulfur cycle before the GOE. Besides, ion probe analyses of microscopic pyrite from carbonates of the Batatal Formation might better constrain the

sulfate-reducing bacteria signal imparted to these minerals. Experiments and modeling can be conducted to explain sulfur and carbon distribution in the Neoarchean using observation of natural processes today.

Bibliography

Anbar, A. D., Duan, Y., Lyons, T. W., Arnold, G. L., Kendall, B., Creaser, R. A., Kaufman, A. J., Gordon, G. W., Scott, C., Garvin, J., et al. A whiff of oxygen before the great oxidation event? *Science*, 317(5846):1903–1906, 2007.

Aspler, L. B. and Chiarenzelli, J. R. Two Neoarchean supercontinents? Evidence from the Paleoproterozoic. *Sedimentary Geology*, 120(1):75–104, 1998.

Babinski, M., Chemale, F., and Van Schmus, W. R. The Pb/Pb age of the Minas Supergroup carbonate rocks, Quadrilátero Ferrífero, Brazil. *Precambrian Research*, 72(3):235–245, 1995.

Bao, H., Rumble III, D., and Lowe, D. R. The five stable isotope compositions of Fig Tree barites: Implications on sulfur cycle in ca. 3.2 Ga oceans. *Geochimica et Cosmochimica Acta*, 71(20):4868–4879, 2007.

Barley, M. E., Bekker, A., and Krapež, B. Late Archean to Early Paleoproterozoic global tectonics, environmental change and the rise of atmospheric oxygen. *Earth and Planetary Science Letters*, 238(1):156–171, 2005.

Barling, J. and Anbar, A. Molybdenum isotope fractionation during adsorption by manganese oxides. *Earth and Planetary Science Letters*, 217(3):315–329, 2004.

Barling, J., Arnold, G., and Anbar, A. Natural mass-dependent variations in the isotopic composition of molybdenum. *Earth and Planetary Science Letters*, 193 (3):447–457, 2001.

Baroni, M., Thiemens, M. H., Delmas, R. J., and Savarino, J. Mass-independent sulfur isotopic compositions in stratospheric volcanic eruptions. *Science*, 315(5808): 84–87, 2007.

Bekker, A., Kaufman, A. J., Karhu, J. A., Beukes, N. J., Swart, Q. D., Coetzee, L. L., and Eriksson, K. A. Chemostratigraphy of the Paleoproterozoic Duitschland Formation, South Africa: implications for coupled climate change and carbon cycling. *American Journal of Science*, 301(3):261–285, 2001.

Bekker, A., Sial, A., Karhu, J., Ferreira, V., Noce, C., Kaufman, A., Romano, A., and Pimentel, M. Chemostratigraphy of Carbonates from the Minas Supergroup, Quadrilátero Ferrífero (Iron Quadrangle), Brazil: A Stratigraphic Record of Early Proterozoic Atmospheric, Biogeochemical and Climactic Change. *American Journal of Science*, 303(10):865–904, 2003.

Bekker, A., Holland, H., Wang, P.-L., Rumble, D., Stein, H., Hannah, J., Coetzee, L., and Beukes, N. Dating the rise of atmospheric oxygen. *Nature*, 427(6970): 117–120, 2004.

Bekker, A., Karhu, J., and Kaufman, A. Carbon isotope record for the onset of the Lomagundi carbon isotope excursion in the Great Lakes area, North America. *Precambrian Research*, 148(1):145–180, 2006.

Berner, R. A. Sedimentary pyrite formation. *American Journal of Science*, 268(1): 1–23, 1970.

Berner, R. A. Sedimentary pyrite formation: an update. *Geochimica et Cosmochimica Acta*, 48(4):605–615, 1984.

Beukes, N. J. and Gutzmer, J. Origin and paleoenvironmental significance of major iron formations at the Archean-Paleoproterozoic boundary. *Society of Economic Geologists Reviews*, 15:5–47, 2008.

Brocks, J. J., Logan, G. A., Buick, R., and Summons, R. E. Archean molecular fossils and the early rise of eukaryotes. *Science*, 285(5430):1033–1036, 1999.

Buchachenko, A. Mass-independent isotope effects. *The Journal of Physical Chemistry B*, 2013.

Canfield, D. E. and Farquhar, J. Animal evolution, bioturbation, and the sulfate concentration of the oceans. *Proceedings of the National Academy of Sciences*, 106(20):8123–8127, 2009.

Canfield, D. E., Farquhar, J., and Zerkle, A. L. High isotope fractionations during sulfate reduction in a low-sulfate euxinic ocean analog. *Geology*, 38(5):415–418, 2010.

Canil, D. Vanadium in peridotites, mantle redox and tectonic environments: Archean to present. *Earth and Planetary Science Letters*, 195(1):75–90, 2002.

Cates, N. L. and Mojzsis, S. J. Chemical and isotopic evidence for widespread Eoarchean metasedimentary enclaves in southern West Greenland. *Geochimica et cosmochimica acta*, 70(16):4229–4257, 2006.

Cheney, E. Sequence stratigraphy and plate tectonic significance of the Transvaal succession of southern Africa and its equivalent in Western Australia. *Precambrian Research*, 79(1):3–24, 1996.

Cloud, P. A working model of the primitive earth. *American Journal of Science*, 272(6):537–548, 1972.

Cloud, P. E. Atmospheric and hydrospheric evolution on the primitive earth. Both secular accretion and biological and geochemical processes have affected earth's volatile envelope. *Science*, 160(3829):729–736, 1968.

Condie, K. C. and ONeill, C. The Archean-Proterozoic boundary: 500 My of tectonic transition in earth history. *American Journal of Science*, 310(9):775–790, 2010.

Coplen, T. B., Hopple, J., Boehike, J., Peiser, H., and Rieder, S. *Compilation of minimum and maximum isotope ratios of selected elements in naturally occurring terrestrial materials and reagents*. US Department of the Interior, US Geological Survey, 2002.

Derry, L. A. and Jacobsen, S. B. The chemical evolution of Precambrian seawater: Evidence from REEs in banded iron formations. *Geochimica et Cosmochimica Acta*, 54(11):2965–2977, 1990.

Des Marais, D. J. Isotopic evolution of the biogeochemical carbon cycle during the Precambrian. *Reviews in Mineralogy and Geochemistry*, 43(1):555–578, 2001.

Dimroth, E. and Kimberley, M. M. Precambrian atmospheric oxygen: evidence in the sedimentary distributions of carbon, sulfur, uranium, and iron. *Canadian Journal of Earth Sciences*, 13(9):1161–1185, 1976.

Domagal-Goldman, S. D., Kasting, J. F., Johnston, D. T., and Farquhar, J. Organic haze, glaciations and multiple sulfur isotopes in the Mid-Archean Era. *Earth and Planetary Science Letters*, 269(1):29–40, 2008.

Dorr, J. Physiographic, stratigraphic and structural development of the Quadrilátero Ferrífero, Minas Gerais, Brazil. *USGS Prof. Pap*, 1969.

Eriksson, P. G. and Cheney, E. S. Evidence for the transition to an oxygen-rich atmosphere during the evolution of red beds in the Lower Proterozoic sequences of southern Africa. *Precambrian research*, 54(2):257–269, 1992.

Farquhar, J. and Wing, B. Multiple sulfur isotopes and the evolution of the atmosphere. *Earth and Planetary Science Letters*, 213(1):1–13, 2003.

Farquhar, J. and Wing, B. A. The terrestrial record of stable sulphur isotopes: a review of the implications for evolution of Earths sulphur cycle. *Geological Society, London, Special Publications*, 248(1):167–177, 2005.

Farquhar, J., Bao, H., and Thiemens, M. Atmospheric influence of Earth's earliest sulfur cycle. *Science*, 289(5480):756–758, 2000.

Farquhar, J., Savarino, J., Airieau, S., and Thiemens, M. Observation of wavelength-sensitive mass-independent sulfur isotope effects during SO_2 photolysis: Implications for the early atmosphere. *Journal of Geophysical Research*, 106(E12): 32829–32, 2001.

Farquhar, J., Wing, B., McKeegan, K., Harris, J., Cartigny, P., and Thiemens, M. Mass-independent sulfur of inclusions in diamond and sulfur recycling on early Earth. *Science*, 298(5602):2369–2372, 2002.

Farquhar, J., Peters, M., Johnston, D. T., Strauss, H., Masterson, A., Wiechert, U., and Kaufman, A. J. Isotopic evidence for Mesoarchaean anoxia and changing atmospheric sulphur chemistry. *Nature*, 449(7163):706–709, 2007.

Farquhar, J., Cliff, J., Zerkle, A. L., Kamyshny, A., Poulton, S. W., Claire, M., Adams, D., and Harms, B. Pathways for Neoarchean pyrite formation constrained by mass-independent sulfur isotopes. *Proceedings of the National Academy of Sciences*, 2013.

Fischer, W., Schroeder, S., Lacassie, J., Beukes, N., Goldberg, T., Strauss, H., Horstmann, U., Schrag, D., and Knoll, A. Isotopic constraints on the Late Archean carbon cycle from the Transvaal Supergroup along the western margin of the Kaapvaal Craton, South Africa. *Precambrian Research*, 169(1):15–27, 2009.

Gaillard, F., Scaillet, B., and Arndt, N. T. Atmospheric oxygenation caused by a change in volcanic degassing pressure. *Nature*, 478(7368):229–232, 2011.

Goericke, R. and Fry, B. Variations of marine plankton $\delta^{13}C$ with latitude, temperature, and dissolved CO_2 in the world ocean. *Global Biogeochemical Cycles*, 8(1): 85–90, 1994.

Guo, Q., Strauss, H., Kaufman, A. J., Schröder, S., Gutzmer, J., Wing, B., Baker, M. A., Bekker, A., Jin, Q., Kim, S.-T., et al. Reconstructing Earth's surface oxidation across the Archean-Proterozoic transition. *Geology*, 37(5):399–402, 2009.

Habicht, K. S., Gade, M., Thamdrup, B., Berg, P., and Canfield, D. E. Calibration of sulfate levels in the Archean ocean. *Science*, 298(5602):2372–2374, 2002.

Halevy, I., Johnston, D. T., and Schrag, D. P. Explaining the structure of the Archean mass-independent sulfur isotope record. *Science*, 329(5988):204–207, 2010.

Harrison, A. and Thode, H. Mechanism of the bacterial reduction of sulphate from isotope fractionation studies. *Transactions of the Faraday Society*, 54:84–92, 1958.

Hartmann, L. A., Endo, I., Suita, M. T. F., Santos, J. O. S., Frantz, J. C., Carneiro, M. A., McNaughton, N. J., and Barley, M. E. Provenance and age delimitation of Quadrilátero Ferrífero sandstones based on zircon U–Pb isotopes. *Journal of South American Earth Sciences*, 20(4):273–285, 2006.

Holland, H. D. *The chemical evolution of the atmosphere and oceans*. Princeton University Press, 1984.

Hu, G., Rumble, D., and Wang, P.-L. An ultraviolet laser microprobe for the in situ analysis of multisulfur isotopes and its use in measuring Archean sulfur isotope mass-independent anomalies. *Geochimica et Cosmochimica Acta*, 67(17):3101–3118, 2003.

Hulston, J. and Thode, H. Variations in the S^{33}, S^{34}, and S^{36} contents of meteorites and their relation to chemical and nuclear effects. *Journal of Geophysical Research*, 70(14):3475–3484, 1965.

James, H. L. Sedimentary facies of iron-formation. *Economic Geology*, 49(3):235–293, 1954.

Johnston, D. T., Wing, B. A., Farquhar, J., Kaufman, A. J., Strauss, H., Lyons, T. W., Kah, L. C., and Canfield, D. E. Active microbial sulfur disproportionation in the Mesoproterozoic. *Science*, 310(5753):1477–1479, 2005.

Johnston, D. T., Poulton, S. W., Fralick, P. W., Wing, B. A., Canfield, D. E., and Farquhar, J. Evolution of the oceanic sulfur cycle at the end of the Paleoproterozoic. *Geochimica et Cosmochimica Acta*, 70(23):5723–5739, 2006.

Kamber, B. and Whitehouse, M. Micro-scale sulphur isotope evidence for sulphur cycling in the late Archean shallow ocean. *Geobiology*, 5(1):5–17, 2007.

Karhu, J. A. and Holland, H. D. Carbon isotopes and the rise of atmospheric oxygen. *Geology*, 24(10):867–870, 1996.

Kasting, J. F. Theoretical constraints on oxygen and carbon dioxide concentrations in the Precambrian atmosphere. *Precambrian research*, 34(3):205–229, 1987.

Kaufman, A. J., Johnston, D. T., Farquhar, J., Masterson, A. L., Lyons, T. W., Bates, S., Anbar, A. D., Arnold, G. L., Garvin, J., and Buick, R. Late Archean biospheric oxygenation and atmospheric evolution. *Science*, 317(5846):1900–1903, 2007.

Kendall, B., Reinhard, C. T., Lyons, T. W., Kaufman, A. J., Poulton, S. W., and Anbar, A. D. Pervasive oxygenation along late Archaean ocean margins. *Nature Geoscience*, 3(9):647–652, 2010.

de Kock, M. O., Evans, D. A., and Beukes, N. J. Validating the existence of Vaalbara in the Neoarchean. *Precambrian Research*, 174(1):145–154, 2009.

Kopp, R. E., Kirschvink, J. L., Hilburn, I. A., and Nash, C. Z. The Paleoproterozoic snowball Earth: a climate disaster triggered by the evolution of oxygenic photosynthesis. *Proceedings of the National Academy of Sciences of the United States of America*, 102(32):11131–11136, 2005.

Kump, L. R., Kasting, J. F., and Barley, M. E. Rise of atmospheric oxygen and the upside-down Archean mantle. *Geochem. Geophys. Geosyst*, 2(1), 2001.

Lasaga, A. C., Otake, T., Watanabe, Y., and Ohmoto, H. Anomalous fractionation of sulfur isotopes during heterogeneous reactions. *Earth and Planetary Science Letters*, 268(1):225–238, 2008.

Laws, E. A., Bidigare, R. R., and Popp, B. N. Effect of growth rate and CO_2 concentration on carbon isotopic fractionation by the marine diatom *Phaeodactylum tricornutum*. *Limnology and Oceanography*, 42:1552–1560, 1997.

Matsuhisa, Y., Goldsmith, J. R., and Clayton, R. N. Mechanisms of hydrothermal crystallization of quartz at 250°C and 15 kbar. *Geochimica et Cosmochimica Acta*, 42(2):173–182, 1978.

McFadden, K. A. and Kelly, A. E. Carbon and sulfur stable isotopic systems and their application in Paleoenvironmental analysis. *Quantifying the Evolution of Early Life*, pages 403–450, 2011.

McLennan, S. M. and Taylor, S. Geochemical constraints on the growth of the continental crust. *The Journal of Geology*, pages 347–361, 1982.

Melezhik, V. A., Fallick, A. E., Medvedev, P. V., and Makarikhin, V. V. Extreme $^{13}C_{carb}$ enrichment in ca. 2.0 Ga magnesite–stromatolite–dolomite–red beds' association in a global context: a case for the world-wide signal enhanced by a local environment. *Earth-Science Reviews*, 48(1):71–120, 1999.

Melezhik, V. A., Fallick, A. E., Rychanchik, D. V., and Kuznetsov, A. B. Palaeoproterozoic evaporites in Fennoscandia: implications for seawater sulphate, the rise of atmospheric oxygen and local amplification of the $\delta^{13}C$ excursion. *Terra Nova*, 17(2):141–148, 2005.

Melnik, Y. Precambrian banded iron-formations, physicochemical conditions of formation. Developments in Precambrian Geology, vol. 5, 1982.

Mojzsis, S. J., Coath, C., Greenwood, J., McKeegan, K., and Harrison, T. Mass-independent isotope effects in Archean (2.5 to 3.8 Ga) sedimentary sulfides determined by ion microprobe analysis. *Geochimica et Cosmochimica Acta*, 67(9): 1635–1658, 2003.

Morford, J. L. and Emerson, S. The geochemistry of redox sensitive trace metals in sediments. *Geochimica et Cosmochimica Acta*, 63(11):1735–1750, 1999.

Nelson, D., Trendall, A., and Altermann, W. Chronological correlations between the Pilbara and Kaapvaal cratons. *Precambrian Research*, 97(3):165–189, 1999.

Nelson, D. R. Granite–greenstone crust formation on the Archaean Earth: a consequence of two superimposed processes. *Earth and Planetary Science Letters*, 158 (3):109–119, 1998.

Nesbitt, H. and Young, G. Early Proterozoic climates and plate motions inferred from major element chemistry of lutites. *Nature*, 299(5885):715–717, 1982.

Oduro, H., Harms, B., Sintim, H. O., Kaufman, A. J., Cody, G., and Farquhar, J. Evidence of magnetic isotope effects during thermochemical sulfate reduction. *Proceedings of the National Academy of Sciences*, 108(43):17635–17638, 2011.

Ohmoto, H. Evidence in pre–2.2 Ga paleosols for the early evolution of atmospheric oxygen and terrestrial biota. *Geology*, 24(12):1135–1138, 1996.

Ohmoto, H., Watanabe, Y., Ikemi, H., Poulson, S. R., and Taylor, B. E. Sulphur isotope evidence for an oxic Archaean atmosphere. *Nature*, 442(7105):908–911, 2006.

Ono, S., Eigenbrode, J. L., Pavlov, A. A., Kharecha, P., Rumble, D., Kasting, J. F., and Freeman, K. H. New insights into Archean sulfur cycle from mass-independent sulfur isotope records from the Hamersley Basin, Australia. *Earth and Planetary Science Letters*, 213(1):15–30, 2003.

Ono, S., Wing, B., Johnston, D., Farquhar, J., and Rumble, D. Mass-dependent fractionation of quadruple stable sulfur isotope system as a new tracer of sulfur biogeochemical cycles. *Geochimica et Cosmochimica Acta*, 70(9):2238–2252, 2006.

Ono, S., Beukes, N. J., and Rumble, D. Origin of two distinct multiple-sulfur isotope compositions of pyrite in the 2.5 Ga Klein Naute Formation, Griqualand West Basin, South Africa. *Precambrian Research*, 169(1):48–57, 2009a.

Ono, S., Kaufman, A. J., Farquhar, J., Sumner, D. Y., and Beukes, N. J. Lithofacies control on multiple-sulfur isotope records and Neoarchean sulfur cycles. *Precambrian Research*, 169(1):58–67, 2009b.

Papineau, D., Mojzsis, S., Coath, C., Karhu, J., and McKeegan, K. Multiple sulfur isotopes of sulfides from sediments in the aftermath of Paleoproterozoic glaciations. *Geochimica et Cosmochimica Acta*, 69(21):5033–5060, 2005.

Partridge, M. A., Golding, S. D., Baublys, K. A., and Young, E. Pyrite paragenesis and multiple sulfur isotope distribution in late Archean and early Paleoproterozoic Hamersley Basin sediments. *Earth and Planetary Science Letters*, 272(1):41–49, 2008.

Pavlov, A. and Kasting, J. Mass-independent fractionation of sulfur isotopes in Archean sediments: strong evidence for an anoxic Archean atmosphere. *Astrobiology*, 2(1):27–41, 2002.

Philippot, P., Van Zuilen, M., Lepot, K., Thomazo, C., Farquhar, J., and Van Kranendonk, M. J. Early Archaean microorganisms preferred elemental sulfur, not sulfate. *Science*, 317(5844):1534–1537, 2007.

Pickard, A. Shrimp U–Pb zircon ages for the Palaeoproterozoic Kuruman Iron Formation, Northern Cape Province, South Africa: evidence for simultaneous BIF deposition on Kaapvaal and Pilbara Cratons. *Precambrian Research*, 125(3): 275–315, 2003.

Popa, R., Kinkle, B. K., and Badescu, A. Pyrite framboids as biomarkers for iron-sulfur systems. *Geomicrobiology Journal*, 21(3):193–206, 2004.

Popp, B. N., Laws, E. A., Bidigare, R. R., Dore, J. E., Hanson, K. L., and Wakeham, S. G. Effect of phytoplankton cell geometry on carbon isotopic fractionation. *Geochimica et Cosmochimica Acta*, 62(1):69–77, 1998.

Raab, M. and Spiro, B. Sulfur isotopic variations during seawater evaporation with fractional crystallization. *Chemical Geology: Isotope Geoscience section*, 86(4): 323–333, 1991.

Ramdohr, P. New observations on the ores of the Witwatersrand in South Africa and their genetic significance. Geological Society of South Africa, 1958.

Rasmussen, B. and Buick, R. Redox state of the Archean atmosphere: evidence from detrital heavy minerals in ca. 3250–2750 Ma sandstones from the Pilbara Craton, Australia. *Geology*, 27(2):115–118, 1999.

Rasmussen, B., Fletcher, I. R., Brocks, J. J., and Kilburn, M. R. Reassessing the first appearance of eukaryotes and cyanobacteria. *Nature*, 455(7216):1101–1104, 2008.

Rau, G. H., Takahashi, T., and Des Marais, D. Latitudinal variations in plankton $\delta^{13}C$: implications for CO_2 and productivity in past oceans. *Nature*, 341(5):165, 1989.

Rees, C. A steady-state model for sulphur isotope fractionation in bacterial reduction processes. *Geochimica et Cosmochimica Acta*, 37(5):1141–1162, 1973.

Rees, C., Jenkins, W., and Monster, J. The sulphur isotopic composition of ocean water sulphate. *Geochimica et Cosmochimica Acta*, 42(4):377–381, 1978.

Rouxel, O., Ono, S., Alt, J., Rumble, D., and Ludden, J. Sulfur isotope evidence for microbial sulfate reduction in altered oceanic basalts at ODP Site 801. *Earth and Planetary Science Letters*, 268(1):110–123, 2008.

Rye, R., Kuo, P. H., and Holland, H. D. Atmospheric carbon dioxide concentrations before 2.2 billion years ago. *Nature*, 378:603–605, 1995.

Rye, R., Holland, H. D., et al. Paleosols and the evolution of atmospheric oxygen: a critical review. *American Journal of Science*, 298(8):621, 1998.

Sagan, C. and Mullen, G. Earth and Mars: evolution of atmospheres and surface temperatures. *Science*, 177(4043):52–56, 1972.

Savarino, J., Romero, A., Cole-Dai, J., Bekki, S., and Thiemens, M. Uv induced mass-independent sulfur isotope fractionation in stratospheric volcanic sulfate. *Geophysical Research Letters*, 30(21):2131, 2003.

Schidlowski, M., Eichmann, R., and Junge, C. E. Carbon isotope geochemistry of the Precambrian Lomagundi carbonate province, Rhodesia. *Geochimica et Cosmochimica Acta*, 40(4):449–455, 1976.

Schoonen, M. A. Mechanisms of sedimentary pyrite formation. *SPECIAL PAPERS-GEOLOGICAL SOCIETY OF AMERICA*, pages 117–134, 2004.

Shen, Y., Farquhar, J., Masterson, A., Kaufman, A. J., and Buick, R. Evaluating the role of microbial sulfate reduction in the early Archean using quadruple isotope systematics. *Earth and Planetary Science Letters*, 279(3):383–391, 2009.

Shen, Y., Farquhar, J., Zhang, H., Masterson, A., Zhang, T., and Wing, B. A. Multiple S-isotopic evidence for episodic shoaling of anoxic water during Late Permian mass extinction. *Nature Communications*, 2:210, 2011.

Sighinolfi, G. P. Geochemistry of early precambrian carbonate rocks from the Brazilian Shield: Implications for archean carbonate sedimentation. *Contributions to Mineralogy and Petrology*, 46(3):189–200, 1974.

Strauss, H. 4 Ga of seawater evolution: Evidence from the sulfur isotopic composition ofsulfate. *Sulfur Biogeochemistry: Past And Present*, (379):195, 2004.

Sumner, D. Y. and Bowring, S. A. U–Pb geochronologic constraints on deposition of the Campbellrand Subgroup, Transvaal Supergroup, South Africa. *Precambrian Research*, 79(1):25–35, 1996.

Ueno, Y., Ono, S., Rumble, D., and Maruyama, S. Quadruple sulfur isotope analysis of ca. 3.5 Ga Dresser Formation: New evidence for microbial sulfate reduction in the early Archean. *Geochimica et Cosmochimica Acta*, 72(23):5675–5691, 2008.

Ueno, Y., Johnson, M. S., Danielache, S. O., Eskebjerg, C., Pandey, A., and Yoshida, N. Geological sulfur isotopes indicate elevated OCS in the Archean atmosphere, solving faint young sun paradox. *Proceedings of the National Academy of Sciences*, 106(35):14784–14789, 2009.

Vorlicek, T. P., Kahn, M. D., Kasuya, Y., and Helz, G. R. Capture of molybdenum in pyrite-forming sediments: role of ligand-induced reduction by polysulfides. *Geochimica et Cosmochimica Acta*, 68(3):547–556, 2004.

Watanabe, Y., Farquhar, J., and Ohmoto, H. Anomalous fractionations of sulfur isotopes during thermochemical sulfate reduction. *Science*, 324(5925):370–373, 2009.

Wignall, P. B. *Black shales*. Clarendon Press Oxford, UK, 1994.

Wilkin, R. and Barnes, H. Formation processes of framboidal pyrite. *Geochimica et Cosmochimica Acta*, 61(2):323–339, 1997.

Williams, H., Hoffman, P. F., Lewry, J. F., Monger, J. W., and Rivers, T. Anatomy of North America: thematic geologic portrayals of the continent. *Tectonophysics*, 187(1):117–134, 1991.

Young, E. D., Galy, A., and Nagahara, H. Kinetic and equilibrium mass-dependent isotope fractionation laws in nature and their geochemical and cosmochemical significance. *Geochimica et Cosmochimica Acta*, 66(6):1095–1104, 2002.

Zerkle, A. L., Claire, M. W., Domagal-Goldman, S. D., Farquhar, J., and Poulton, S. W. A bistable organic-rich atmosphere on the Neoarchaean Earth. *Nature Geoscience*, 5(5):359–363, 2012.